HHS Public Access

Author manuscript

Cell Rep. Author manuscript; available in PMC 2022 August 29.

Published in final edited form as:

Cell Rep. 2022 August 16; 40(7): 111222. doi:10.1016/j.celrep.2022.111222.

A central alarm system that gates multi-sensory innate threat cues to the amygdala

Sukjae J. Kang[1,9], **Shijia Liu**[1,2,9], **Mao Ye**[1], **Dong-Il Kim**[1], **Gerald M. Pao**[3,4], **Bryan A. Copits**[5,6], **Benjamin Z. Roberts**[7], **Kuo-Fen Lee**[1], **Michael R. Bruchas**[8], **Sung Han**[1,2,7,10,*]

[1]Peptide Biology Laboratory, The Salk Institute for Biological Studies, La Jolla, CA 92037, USA

[2]Department of Neurobiology, School of Biological Sciences, University of California, San Diego, La Jolla, CA 92093, USA

[3]Molecular and Cellular Biology Laboratory, The Salk Institute for Biological Studies, La Jolla, CA 92037, USA

[4]Okinawa Institute of Science and Technology Graduate University, 1919-1 Tancha, Onna-son, Okinawa 904-0495, Japan

[5]Washington University Pain Center, Washington University School of Medicine, St. Louis, MO 63110, USA

[6]Department of Anesthesiology, Washington University School of Medicine, St. Louis, MO 63110, USA

[7]Neurosciences Graduate Program, University of California, San Diego, La Jolla, CA 92093, USA

[8]Center of Excellence in the Neurobiology of Addiction, Pain, and Emotion, Departments of Anesthesiology and Pain Medicine, and Pharmacology, University of Washington, Seattle, WA 98195, USA

[9]These authors contributed equally

[10]Lead contact

SUMMARY

Perception of threats is essential for survival. Previous findings suggest that parallel pathways independently relay innate threat signals from different sensory modalities to multiple brain areas, such as the midbrain and hypothalamus, for immediate avoidance. Yet little is known

*Correspondence: sunghan@salk.edu.

AUTHOR CONTRIBUTIONS

S.H. conceived of the idea and secured funding. S.H., S.J.K., S.L., and M.Y. designed the experiments. S.L., S.H., and S.J.K. wrote the manuscript. S.J.K. performed most $CGRP^{SPFp}$ experiments. S.L. and S.J.K. performed most $CGRP^{PBel}$ experiments. S.L. set up the miniscope experiment and analyzed the data. M.Y. performed electrophysiology and $CGRP^{PBel}$ RTPA. D.-I.K. provided viruses. G.M.P. performed the CCM analyses. K.-F.L. provided resources for microscopy. M.R.B. and B.A.C. provided the PPO virus. B.Z.R. edited the manuscript.

DECLARATION OF INTERESTS

The authors declare no competing interests.

SUPPLEMENTAL INFORMATION

Supplemental information can be found online at https://doi.org/10.1016/j.celrep.2022.111222.

about whether and how multi-sensory innate threat cues are integrated and conveyed from each sensory modality to the amygdala, a critical brain area for threat perception and learning. Here, we report that neurons expressing calcitonin gene-related peptide (CGRP) in the parvocellular subparafascicular nucleus in the thalamus and external lateral parabrachial nucleus in the brainstem respond to multi-sensory threat cues from various sensory modalities and relay negative valence to the lateral and central amygdala, respectively. Both CGRP populations and their amygdala projections are required for multi-sensory threat perception and aversive memory formation. The identification of unified innate threat pathways may provide insights into developing therapeutic candidates for innate fear-related disorders.

Graphical Abstract

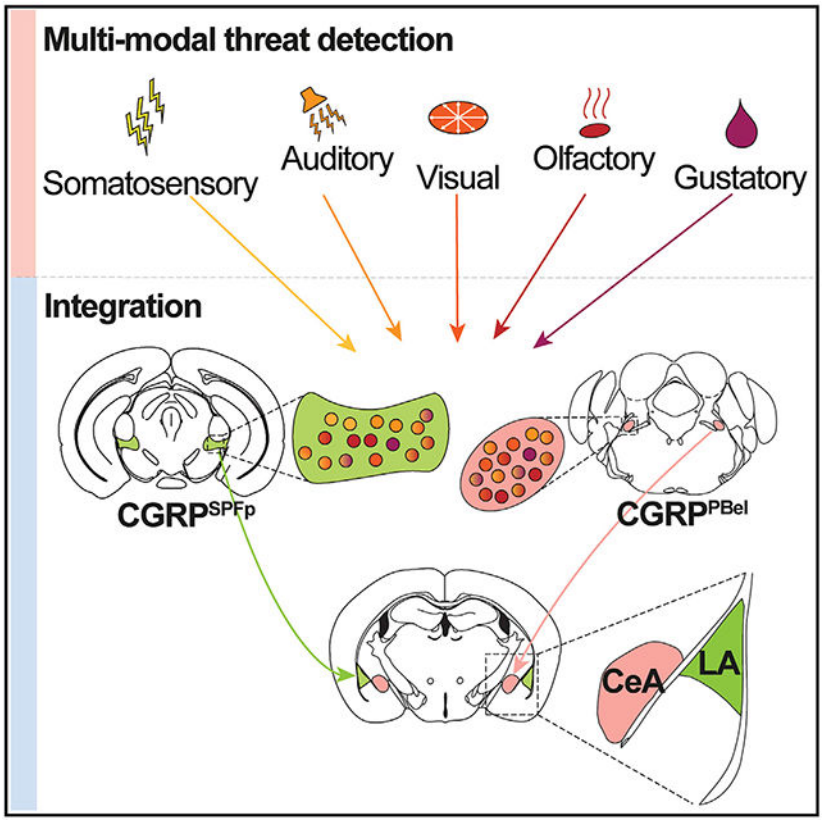

In brief

Kang et al. report that two CGRP-expressing neuronal populations in the thalamus and brainstem are activated by innate threat cues from various sensory modalities and are required for their perception. These CGRP neurons relay multi-sensory threat cues to the lateral and central amygdala, forming two parallel pathways for aversive memory formation.

INTRODUCTION

To survive in nature, animals must quickly react to danger by detecting aversive information from multiple sensory modalities, such as the shadow of an eagle or the sound of a

rattlesnake. Multi-sensory threat stimuli are thought to be detected and processed in parallel by a wide range of relay stations (Silva et al., 2016). To date, separate neural pathways have been reported for processing aversive somatosensory (Barsy et al., 2020; Choi et al., 2020; Han et al., 2015; Sato et al., 2015), visual (Salay et al., 2018; Wei et al., 2015; Zhou et al., 2019), auditory (Barsy et al., 2020; Li et al., 2021; Zhang et al., 2018), gustatory (Carter et al., 2013; Kim et al., 2017; Wang et al., 2018), and olfactory (Rosen et al., 2015; Tong et al., 2020) stimuli and generating immediate defensive behavioral/physiological responses. A common neural substrate that integrates aversive cues from various sensory modalities would be beneficial for survival because essentially all threats in nature exist as multi-modal aversive sensory cues. In addition, it would facilitate efficient information processing and timely initiation of behavioral responses by delivering unified scalable alarm signals to the brain. However, the existence of such pathways has yet to be established.

One candidate brain region for the integration of multi-sensory threat information is the amygdala, a well-known limbic structure crucial for initiating behavioral responses to environmental stimuli and forming associative memories (Janak and Tye, 2015; LeDoux, 2000, 2012). The role of the amygdala in processing aversive information of multiple sensory modalities has been suggested. For example, during canonical Pavlovian threat conditioning, the amygdala is activated by both aversive somatosensory stimuli (e.g., foot shock) and paired auditory cues (Ren and Neugebauer, 2010; Simons et al., 2014; Veinante et al., 2013). Furthermore, lesioning the amygdala attenuates the responsivity to sensory threats from visual (Bach et al., 2015; Blanchard and Blanchard, 1972; Dal Monte et al., 2015), auditory (Scott et al., 1997), and somatosensory (Blanchard and Blanchard, 1972) modalities, and humans with bilateral damage to this structure exhibit no fear responses to any external threat except CO_2 (Feinstein et al., 2011). Finally, the formation of aversive memories involving multi-sensory innate threats is amygdala dependent (Blanchard and Blanchard, 1972), supporting the existence of pathways that convey multi-modal aversive sensory cues to the amygdala. However, the neural circuitry that encodes multi-sensory innate aversive cues (other than foot shock) to the amygdala during aversive learning remains uninvestigated.

The amygdala receives dense presynaptic inputs from the posterior thalamus (Craig et al., 1994, 2000; Gauriau and Bernard, 2004; Price, 2002) and the parabrachial nucleus (Usunoff et al., 2006), relay centers that process innate and learned signals of several sensory modalities (e.g., auditory [Yasui et al., 1992], somatosensory [Nakamura and Morrison, 2008], and gustatory [Jarvie et al., 2021]). Subregions of these areas, the parvocellular subparafascicular nucleus (SPFp; also referred to as the posterior thalamus or posterior intralaminar nucleus in the thalamus) (D'Hanis et al., 2007; Dobolyi et al., 2005; Kruger et al., 1988) and external lateral parabrachial nucleus (PBel), highly express calcitonin gene-related peptide (CGRP), a neuropeptide associated with aversion and nociception (Palmiter, 2018; Russell et al., 2014; Russo, 2015; Shinohara et al., 2017; Yu et al., 2009). In particular, CGRP neurons in the PBel mediate aversive memory formation by transmitting somatosensory and visceral signals to the central amygdala (CeA) (Campos et al., 2018; Chen et al., 2018; Han et al., 2015). CGRP neurons in the medial SPFp are involved in sexual behaviors (Coolen et al., 2003a, 2003b), whereas those in the posterolateral SPFp have been reported to send projections to the lateral amygdala (LA) and striatal amygdala

(AStr), implicating that they may be involved in aversive learning (D'Hanis et al., 2007; LeDoux et al., 1985; Yasui et al., 1991). However, the functional role of these neurons in aversive learning has not been investigated.

Given these findings, we hypothesized that CGRP neurons relay multi-sensory innate threat information to the amygdala and that these circuits are involved in generating appropriate behavioral responses and forming aversive memories of innate threat cues.

Here, we report two distinct neural populations in the thalamus and the brainstem, the $CGRP^{SPFp}$ and $CGRP^{PBel}$ neurons, that project to non-overlapping amygdalar subnuclei. These two CGRP populations encode aversive sensory stimuli from various modalities (visual, auditory, somatosensory, gustatory, and olfactory) by recruiting distinct local networks. Silencing $CGRP^{SPFp}$ or $CGRP^{PBel}$ neurons and their terminals in the LA or CeA attenuate the perception of aversive multi-sensory stimuli. Lastly, both the $CGRP^{SPFp\rightarrow LA}$ and $CGRP^{PBel\rightarrow CeA}$ circuits are critical for aversive memory formation. The discovery of parallel multi-sensory innate threat pathways supports the critical role of the amygdala in priming behavioral responses to a broad scope of environmental challenges.

RESULTS

Multi-sensory threat stimuli activate $CGRP^{SPFp}$ and $CGRP^{PBel}$ neurons

To investigate how $CGRP^{SPFp}$ and $CGRP^{PBel}$ neurons respond to multi-sensory innate threat stimuli, we recorded the activities of both populations with miniscope single-cell calcium imaging (Figures 1A and 1B) while presenting multi-sensory innate threat stimuli to freely moving mice (Figure 1C). We expressed jGCaMP8m (Zhang et al., 2020) Cre-dependently in the SPFp or PBel of $Calca^{Cre}$ mice (The *Calca* gene encodes CGRP) and implanted a gradient-index (GRIN) lens to facilitate *in vivo* recording of single neuron activities. Mice were presented with aversive threat stimuli of somatosensory (0.2 mA, 2 s foot shock), auditory (85 dB, 2 s sound burst, mimicking thunder blast), visual (2 s expanding looming disk, mimicking the rapid approach of avian predators), olfactory (exposure to cotton tip with 10 μL of trimethylthiazoline [TMT], a constituent of fox feces), and gustatory modalities (presentation of 10 μL of 0.5 mM quinine solution to water-restricted mice).

Out of 80 $CGRP^{SPFp}$ (Figure 1D) and 80 $CGRP^{PBel}$ neurons (Figure 1F) recorded, most increased their activity upon presentation of aversive, but not control, stimuli (Figures S2A and S2B), with many neurons responding to more than one sensory modality (Figures 1E and 1G; Tables S1 and S2). Interestingly, we observed different clusters of neurons that preferentially responded to aversive stimuli of each sensory modality. Thus, we sought to further compare the neurons recruited by five modalities using a manifold-based algorithm called convergent cross-mapping (CCM) (Sugihara et al., 2012). Here, CCM is used as a more sophisticated measure than cross-correlation to describe the similarity between the manifolds of the embedded time series of each neuron pair instead of just the cross-correlation of the raw time series, allowing us to compare the neurons recruited across different sensory modalities.

We first calculated the prediction score between each pair of neurons using their peri-stimulus activity traces. A prediction score ρ ($\Sigma obs_{(1,2,\ldots n)}/\Sigma pred_{(1,2,\ldots n)}$) of 1 indicates that the activity of the input neuron can perfectly predict the future activity of the output neuron. We then performed hierarchical clustering on the prediction score matrix for each of the five stimuli (Figures S2C and S2D, diagonal matrices); clusters represented activated network motifs, since they were composed of neurons that shared the "broadcasters" and "receivers." However, when we used the same index in the "seed" clustergram to plot the other four heatmaps (Figures S2C and S2D), the clusters were no longer preserved and the heatmaps became dissimilar to each other as quantified by the distance matrix (Figures S2E and S2F), thus indicating that network motifs recruited by each of the five sensory modalities are also distinct. Together, these results suggest that aversive stimuli of all five modalities tested activate $CGRP^{SPFp}$ or $CGRP^{PBel}$ neurons and that each stimulus recruits unique combinations of neurons with distinct patterns of information sharing.

CGRP neurons receive inputs from sensory relay areas

To explore the possible sources of multi-sensory inputs to the $CGRP^{SPFp}$ and the $CGRP^{PBel}$ neurons, we performed the monosynaptic retrograde rabies tracing experiment (Kim et al., 2016) (Figure 2A). Both $CGRP^{SPFp}$ and $CGRP^{PBel}$ neurons received inputs from various sensory relay areas, including the superior colliculus (for visual information), inferior colliculus (for auditory information), vestibular nucleus (for proprioceptive information), spinal dorsal horn (for somatosensory information), trigeminal spinal nucleus (for somatosensory information from the face), and the hypothalamus (e.g., zona incerta [ZI] and lateral hypothalamus [LHA] for multi-sensory information) (Figures 2B-2D, S3A, and S3B; Tables S3 and S4). Furthermore, these two CGRP populations displayed different input profiles. While $CGRP^{SPFp}$ neurons received dense inputs from the midbrain (superior and inferior colliculus), $CGRP^{PBel}$ neurons received abundant projections from the amygdala (in particular the CeA), hypothalamus (ZI, LHA, and parasubthalamic nucleus), and brainstem structures (nucleus tractus solitarius and reticular formation). These different input profiles suggest that these two CGRP populations may serve different roles in innate threat perception.

CGRP neurons are required for multi-sensory innate threat perception

Since both $CGRP^{SPFp}$ and $CGRP^{PBel}$ neurons can be activated by multi-sensory innate threat stimuli, we next explored whether they are required for multi-sensory threat perception. To this end, we silenced both populations by expressing tetanus toxin light chain (TetTox) bilaterally in the SPFp or PBel of $Calca^{Cre}$ mice and measured behavioral responses to multi-modal threat stimuli (Figure 3A). Freezing responses to electric foot shock (Figure 3B) and high-intensity sound bursts (Figure 3C) were significantly reduced in both the $CGRP^{SPFp}$ and $CGRP^{PBel}$ TetTox groups compared with the EYFP control groups. While freezing responses to overhead looming stimuli were attenuated in the $CGRP^{SPFp}$ TetTox group compared with controls, the $CGRP^{PBel}$ TetTox group did not differ from controls (Figure 3D).

To assess olfactory threat responses, we next performed a two-chamber preference test in which animals' preference between two chambers containing water and TMT was measured.

Silencing CGRP^{SPFp} neurons did not affect animals' avoidance of TMT, whereas this phenotype was abolished in the CGRP^{PBel} TetTox group (Figure 3E). Lastly, gustatory threat response was assessed using a two-bottle choice test in which preference between water and quinine was measured in overnight-water-restricted animals. Quinine aversion was significantly reduced in the CGRP^{PBel} TetTox group but not the CGRP^{SPFp} TetTox group (Figure 3F). Interestingly, although the CGRP^{SPFp} neurons were activated by TMT and quinine (Figure 1D) and CGRP^{PBel} neurons were activated by looming (Figure 1F), inhibition of these populations individually was not sufficient to attenuate the corresponding threat responses, presumably because of the existence of redundant pathways. These results indicate that CGRP^{SPFp} and CGRP^{PBel} neurons are required for mediating behavioral responses to different sets of multi-sensory threats.

CGRP^{SPFp} and CGRP^{PBel} neurons relay negative valence to the amygdala

The amygdala is implicated in both threat perception and multi-sensory information processing (Bach et al., 2015; Blanchard and Blanchard, 1972; LeDoux, 2000; Ren and Neugebauer, 2010; Scott et al., 1997), so we investigated whether both CGRP populations mediate multi-sensory threat perception via their projections to the amygdala. We first characterized the projections from CGRP^{SPFp} and CGRP^{PBel} neurons to the amygdala by expressing EYFP or mCherry in both populations in the same animals (Figure 4A). Interestingly, EYFP-expressing CGRP^{SPFp} terminals and mCherry-expressing CGRP^{PBel} terminals in the amygdala were mutually exclusive (Figure 4B). While CGRP^{SPFp} synaptic terminals were found in the LA, AStr, and medial amygdala, CGRP^{PBel} terminals were most abundant in the CeA and basomedial amygdala (Figure S3C). Non-amygdalar projections from both CGRP populations were also distinct. CGRP^{SPFp} neurons projected to the auditory cortex and dorsal posterior insular cortex (pIC) and did not project to the somatosensory cortex, whereas CGRP^{PBel} neurons projected to the bed nuclei of the stria terminalis, the ventral posteromedial nucleus of the thalamus (parvicellular part), the parasubthalamic nucleus, and the ventral pIC (Figure S3D). Together, these data suggest that the two populations of CGRP neurons are uniquely positioned to anatomically receive aversive sensory stimuli from a wide range of modalities and relay them to the amygdala.

The CGRP$^{PBel\rightarrow CeA}$ circuit encodes unconditioned noxious stimuli (i.e., foot shock) during aversive learning (Bowen et al., 2020; Han et al., 2015), yet the projections of CGRP^{SPFp} neurons to the amygdala have not been functionally characterized. Since CGRP^{SPFp} neurons project to the LA (Figure 4B), a key area of neural plasticity during threat learning (LeDoux, 2000), we sought to characterize the functional connectivity of this circuit and some other regions (AStr and pIC) via slice electrophysiology and optogenetics. We first expressed channelrhodopsin-2 (ChR2) in the CGRP^{SPFp} neurons and performed electrophysiology recording in the AStr, pIC, and LA (Figures S4A and S4B). We observed optogenetically evoked excitatory (EPSCs) and inhibitory postsynaptic currents (IPSCs) in AStr, pIC, and LA neurons (Figure S4C; pIC trace not shown). Both currents were blocked by the AMPA receptor antagonist CNQX, suggesting the existence of glutamatergic synapses (Figure S4C). Moreover, while most synapses contained both excitatory and inhibitory components (Figure S4D), the onset of IPSCs lagged 4–5 ms relative to EPSCs, indicating the existence

of a feedforward inhibitory circuit (Figures S4E-S4G). The amplitudes of optogenetically evoked EPSCs (Figure S4H) or IPSCs (Figure S4I) in the three regions were similar.

Next, we tested whether $CGRP^{SPFp}$ neurons encode negative valence and relay it to the downstream regions, including the LA, using a real-time place aversion (RTPA) test. Mice were placed in a two-chamber arena, one side of which was paired with photostimulation of $CGRP^{SPFp}$ cell bodies (Figure 4C) or $CGRP^{SPFp}$ terminals, including the $CGRP^{SPFp\rightarrow LA}$ projection (Figures 4F and S4J). In both experiments, the ChR2 group, but not EYFP controls, avoided the photostimulation-paired chamber (Figures 4D, 4E, 4G, 4H, S4J, S5A, and S5B). We used a similar RTPA paradigm to investigate whether $CGRP^{PBel}$ neurons similarly encode negative valence and transmit this information to the CeA. Photostimulation of $CGRP^{PBel}$ cell bodies (Figures 4I-4K and S5C) and $CGRP^{PBel\rightarrow CeA}$ terminals (Figures 4L-4N and S5D) both induced aversion to the light-paired chamber. Together, these results suggest that $CGRP^{SPFp}$ and $CGRP^{PBel}$ neurons relay negative valence to non-overlapping amygdala subnuclei.

$CGRP^{SPFp\rightarrow LA}$ and $CGRP^{PBel\rightarrow CeA}$ projections are required for multi-sensory threat perception

Given that both CGRP neuronal populations, together with their projections to the amygdala, are required for multi-sensory innate threat responses, we next investigated whether $CGRP^{SPFp\rightarrow LA}$ and $CGRP^{PBel\rightarrow CeA}$ circuits are also necessary for generating threat responses to multi-sensory aversive signals. We used, respectively, a photoswitchable Gi-coupled opsin that directly inhibits transmitter release, parapinopsin (PPO) (Copits et al., 2021) (Figure 5A), and a light-driven outward proton pump, archaerhodopsin (ArchT) (Figure 5F), to optogenetically inhibit the axon terminals of $CGRP^{SPFp\rightarrow LA}$ and $CGRP^{PBel\rightarrow CeA}$ projections while presenting the same threat stimuli used in the cell-body inhibition experiment.

Silencing the $CGRP^{SPFp\rightarrow LA}$ pathway attenuated freezing responses to auditory (Figure 5B) and visual (Figure 5C) stimuli compared with controls but did not alter responses to olfactory (Figure 5D) or gustatory (Figure 5E) stimuli. Meanwhile, silencing the $CGRP^{PBel\rightarrow CeA}$ pathway attenuated defensive behavior following the presentation of auditory (Figure 5G), olfactory (Figure 5I), and gustatory (Figure 5J) stimuli, but not visual stimuli (Figure 5H). The somatosensory stimulus (electric foot shock) was excluded here because it will be discussed in the following section. These results are consistent with the cell-body silencing experiment (Figure 3), indicating the critical roles of both $CGRP^{PBel\rightarrow CeA}$ and $CGRP^{SPFp\rightarrow LA}$ circuits in generating innate responses to multi-sensory threat cues.

$CGRP^{SPFp\rightarrow LA}$ and $CGRP^{PBel\rightarrow CeA}$ projections are required for threat memory formation but not expression

Since both $CGRP^{SPFp\rightarrow LA}$ and $CGRP^{PBel\rightarrow CeA}$ circuits are critical for generating behavioral responses to multi-sensory threat signals, we next tested whether they are similarly important for threat memory formation. We used miniscope single-cell calcium imaging to quantify the recruitment of $CGRP^{SPFp}$ neurons during a traditional Pavlovian

threat-conditioning paradigm that coupled auditory cues with foot shock. Animals displayed minimal freezing during habituation (Figure S6A), but prominent freezing behavior during both the conditioning phase and the cue-dependent retrieval test (Figures S6B and S6C). $CGRP^{SPFp}$ neurons were activated by foot shock (Figure 6A, middle panel) but not by tones during habituation or the cue test (Figures 6A and 6B). These data suggest that $CGRP^{SPFp}$ neurons encode somatosensory threats (unconditioned stimulus [US]) during threat conditioning but do not play a role in their association with conditioned stimuli.

We next performed a projection-specific optogenetic conditioning test wherein $CGRP^{SPFp}$ terminal photostimulation, including the $CGRP^{SPFp\rightarrow LA}$ projection, was used as the US in lieu of foot shock. In the context-dependent retrieval test, the $CGRP^{SPFp\rightarrow LA}$ ChR2 group exhibited more freezing than the control while the $CGRP^{SPFp\rightarrow AStr}$ or $CGRP^{SPFp\rightarrow pIC}$ ChR2 group did not (Figures 6C, S4K, and S7A). All the projection ChR2 groups formed memory in the cue-dependent test, but only the $CGRP^{SPFp\rightarrow LA}$ and $CGRP^{SPFp\rightarrow pIC}$ ChR2 group froze more than the control during the tone exposure. Moreover, the $CGRP^{SPFp\rightarrow LA}$ ChR2 group exhibited more freezing than the $CGRP^{SPFp\rightarrow AStr}$ ChR2 group (Figures 6D and S4L). These results indicate that $CGRP^{SPFp\rightarrow LA}$ activation was sufficiently aversive to act as the US and induce a fear memory rather than stimulating the other projection regions. Thus, we did not further pursue AStr and pIC in the terminal inhibition experiments. Lastly, we silenced the $CGRP^{SPFp\rightarrow LA}$ pathway with PPO during the conditioning phase of the traditional threat-conditioning paradigm. Both groups showed similar aversive behavior (jumping and freezing) during the conditioning (data not shown), indicating that inhibition of the amygdalar projection was not able to attenuate the immediate response to the strong somatosensory stimuli. However, compared with controls, PPO-expressing animals displayed reduced freezing behavior in both the context- and cue-dependent fear retrieval tests (Figures 6E, 6F, and S7B). When silencing the same circuit only during the retrieval sessions after threat conditioning, no reductions of freezing were observed (Figures S7E-S7G), indicating that these circuits are necessary for relaying US information but not for memory retrieval.

$CGRP^{PBel}$ neurons were similarly activated by only the US during threat conditioning (Figures 6G, 6H, and S6D-S6F). Some neurons from the same field of view displayed similar activity patterns but were confirmed to be spatially segregated (Figures S6G-S6J). $CGRP^{PBel\rightarrow CeA}$ photostimulation was like-wise sufficient to generate an aversive memory during optogenetic conditioning, increasing freezing behavior in both the context (Figures 6I and S7C) and cue retrieval tests (Figure 6J). Inhibiting the $CGRP^{PBel\rightarrow CeA}$ projection during the conditioning phase of the traditional threat-conditioning paradigm with ArchT reduced freezing behavior during the cue test (Figure 6L), but not the context test (Figures 6K and S7D). Moreover, inhibiting this circuit only during the retrieval tests did not alter freezing responses (Figures S7H-S7J), thus indicating that it is not required for threat memory expression.

Collectively, these data suggest that both $CGRP^{SPFp\rightarrow LA}$ and $CGRP^{PBel\rightarrow CeA}$ circuits are crucial for forming aversive memories by relaying US information.

DISCUSSION

Regardless of sensory modality, it is critical that threat stimuli be processed promptly and reliably to elicit appropriate behavioral responses. The present study characterized two parallel circuits that encode multi-sensory innate threat signals and are required for innate defensive behaviors. These two circuits comprise thalamic (SPFp) and brainstem (PBel) CGRP neurons that project to complementary subdivisions of the amygdala, a well-known center for generating threat memories and diverse defensive responses. $CGRP^{SPFp}$ neurons send massive projections to AStr and LA, making it difficult to manipulate just one region. However, we have performed experiments with different optic fiber positions (Figures S4M and S4N), allowing us to confidently claim the role of the $CGRP^{SPFp \rightarrow LA}$ circuit in our study.

Both $CGRP^{SPFp}$ and $CGRP^{PBel}$ neurons are activated by threat signals of all five modalities tested (Figure 1). Interestingly, different subpopulations of neurons are preferentially recruited by each modality, possibly encoding stimulus identity (Figures 1D, 1F, and S2C-S2F). Although both $CGRP^{SPFp \rightarrow LA}$ and $CGRP^{PBel \rightarrow CeA}$ circuits are necessary for processing somatosensory and auditory threat cues, aversive visual stimuli require only the former pathway for processing while olfactory and gustatory stimuli require only the latter. This specificity may originate from distinct input patterns (Figure 2). $CGRP^{SPFp}$ neurons receive densest inputs from midbrain visual and auditory centers (i.e., the superior and inferior colliculi [Silva et al., 2016; Zhou et al., 2019]), while $CGRP^{PBel}$ neurons receive inputs from the nucleus tractus solitarius, a key player in gustatory and olfactory processing (Garcia-Diaz et al., 1988). Additionally, terminal optogenetic inhibition did not influence the immediate defensive responses by foot shock. Based on these distinctions, we speculate that the $CGRP^{SPFp \rightarrow LA}$ circuit is more specialized for processing exteroceptive signals while the $CGRP^{PBel \rightarrow CeA}$ circuit is more specialized for processing interoceptive stimuli. Moreover, we contemplate that both circuits are necessary for aversive memory formation, but they have limited effects in immediate escape responses associated with bursts of locomotor activity by intense stimuli such as jumping and running. Other parallel circuits may be mediating those immediate responses by severe stimuli (Chiang et al., 2020; Silva et al., 2016). Another interesting possibility we have yet to rule out is that both circuits could relay appetitive information to the amygdala in addition to aversive information.

A shared neural substrate for encoding multi-modal aversive sensory signals would confer many advantages for survival. First, given that predators often generate stimuli of multiple sensory modalities simultaneously, the convergence of these threat signals onto a single brain area could facilitate decision-making and the initiation of appropriate responses. CGRP neurons from the SPFp and PBel may serve as parallel conduits of sensory information from various upstream regions to the amygdala, which can then mediate the behavioral and physiological components of the fear responses via downstream targets (e.g., periaqueductal gray [Rizvi et al., 1991] or hypothalamus [Viviani et al., 2011]). Second, a shared circuit for detecting multi-sensory innate threats could be integrated into the network for aversive memory formation. Here, we demonstrated that: (1) the $CGRP^{SPFp \rightarrow LA}$ and $CGRP^{PBel \rightarrow CeA}$ circuits are necessary for forming threat memories in response to foot shock during Pavlovian threat learning; (2) the same pathways that process foot-shock cues relay

innate threat cues from other sensory modalities; (3) stimulation of either of these pathways is sufficient to act as a US. These same pathways are therefore likely recruited when forming memories of innate sensory threats. Our findings complement the current understanding of innate threat perception circuitry whereby threat cues from each sensory modality are processed in parallel by different brain areas (Canteras, 2002; Gross and Canteras, 2012; Kunwar et al., 2015; Silva et al., 2013) independently from the Pavlovian threat learning circuit (Silva et al., 2016). Finally, a common neural substrate for multiple threat signals could be an entry point for coordinating threat responses with other behaviors. For example, the amygdala could be modulated by various inputs (Fu et al., 2020) and allow threat signals to be collectively regulated with other behavior demands, e.g., foraging and parental drives (Comeras et al., 2019; Ferreira et al., 2002). However, our terminal inhibition of the $CGRP^{PBel \rightarrow CeA}$ circuit was not able to attenuate the freezing behavior during the context test of the threat-conditioning experiment. This phenomenon could be due to the intricacies of the contextual and cued threat-conditioning paradigms. Previous studies claim that the contextual fear conditioning requires both hippocampus and amygdala, while cued threat conditioning is amygdala dependent but hippocampus independent (Kim and Fanselow, 1992; Nagy et al., 2006). Therefore, terminal inhibition of the $CGRP^{PBel \rightarrow CeA}$ circuit may not affect contextual freezing.

Our study suggests that the neuropeptide CGRP may be a marker for circuits that process multi-sensory innate threat stimuli. Importantly, it has also been shown that CGRP exerts functional roles in the amygdala. For example, infusing CGRP receptor antagonist into the CeA blocks Pavlovian auditory fear conditioning (Kocorowski and Helmstetter, 2001). Future developments of *in vivo* CGRP release monitoring approaches are needed to unveil the contributions of CGRP in the circuits reported here. In humans, the PBel and SPFp also abundantly express CGRP (Lacalle and Saper, 2000), suggesting that the dual circuits we reported in mice may also be involved in threat perception-related psychiatric disorders. For example, the CGRP signaling pathway is a proven therapeutic target for migraines (Ashina, 2020), which involve hypersensitivity toward neutral stimuli (Demarquay and Mauguière, 2016; Harriott and Schwedt, 2014). It is, therefore, likely that the CGRP network, including the two populations reported in this study, are also hyperactive during migraine-triggered sensory hypersensitivity episodes. CGRP receptorantagonistsor neutralizing monoclonal antibodies currently used for migraines may also be useful for treating other disorders involving multi-sensory stimuli processing abnormalities, including autism (Nelson et al., 2001), post-traumatic stress disorder (Ashina et al., 2020), and chronic pain disorders such as fibromyalgia (Harte et al., 2016; López-Solà et al., 2017). Examining the roles of CGRP signaling in the $CGRP^{SPFp \rightarrow LA}$ and $CGRP^{PBel \rightarrow CeA}$ circuits in mediating migraine-related symptoms would be an exciting direction for further research.

Limitations of the study

We would like to point out several aspects of our current study that are worth further investigation. First, results from our study are at discrepancy with a previous study regarding the $CGRP^{PBel}$ neurons' role in the cue retrieval test (Campos et al., 2018). While our results show that no net calcium activity changes in $CGRP^{PBel}$ neurons were observed during cue retrieval, Campos et al. showed increased $CGRP^{PBel}$ activity in response to the

conditioned stimulus during the memory retrieval test, which were decreased as the animal was repeatedly exposed to the tone. We believe that this discrepancy could be due to the intensity of the tone, since our study used a low-intensity conditioned stimulus (73 dB tone) that does not activate $CGRP^{PBel}$ neurons during conditioning. However, we would need to perform a fear conditioning experiment with a higher-intensity auditory conditioned stimulus cue to draw this conclusion. Although we showed that the $CGRP^{PBel}$ neuronal activation is not necessary for memory retrieval (Figures S7I and S7J), future studies will be needed to evaluate whether different conditioned stimulus intensities contribute differentially to the role of $CGRP^{PBel}$ neurons in associative threat learning. Second, we did not identify specific cell types of the LA or CeA neurons that receive inputs from the SPFp or PBel in these circuits. The neurons responsible for these functions in the CeA express CGRP receptor (Han et al., 2015), but their counterparts in the LA have not been characterized, which remains an open question for follow-up studies. Finally, our study shows that the $CGRP^{SPFp\rightarrow LA}$ and $CGRP^{PBel\rightarrow CeA}$ circuits serve the parallel US pathways in foot-shock-induced classical threat learning. Considering that these parallel circuits relay multi-sensory threat signals to the amygdala, it is plausible that they play similar roles in forming aversive memories associated with other sensory threat cues. However, this idea was not tested in the current study and requires further investigation.

STAR★METHODS

RESOURCE AVAILABILITY

Lead contact—Further information and requests for resources and reagents should be directed to and will be fulfilled by the lead contact, Sung Han (sunghan@salk.edu).

Materials availability—This study did not generate new unique reagents.

Data and code availability

- All data reported in this paper will be shared by the lead contact upon request.
- All original code has been deposited at Zenodo and is publicly available as of the date of publication. DOIs are listed in the key resources table.
- Any additional information required to reanalyze the data reported in this paper is available from the lead contact upon request.

EXPERIMENTAL MODEL AND SUBJECT DETAILS

Mouse lines—All protocols for animal experiments were approved by the IACUC of the Salk Institute for Biological Studies according to NIH guidelines for animal experimentation. The *Calca*^{Cre}, transgenic mouse line (expressing Cre-GFP fusion protein in CGRP positive neurons) used in this study was generated from the Richard Palmiter's laboratory (Carter et al., 2013) and backcrossed with C57Bl/6J for >6 generations. GFP expression from the Cre-GFP fusion protein is undetectable in perfused slices, in sharp contrast with the fluorescence from viral expression (see Figure S1 for example slices of AAV-DIO-jGCaMP8m unilateral expression). 8–12-week-old male and female mice were used in all studies. Animals were randomized to experimental groups and no sex differences

were noted. Mice were maintained on a normal 12-hour light/dark cycle and provided with food and water *ad libitum.*

METHOD DETAILS

Stereotaxic surgery for virus injection and optic fiber implantation—Mice were anesthetized by isoflurane gas anesthesia (induction at 3.5%, maintenance at 1.5-2%; Dräger Vapor® 2000, Draeger). Mice were then placed on a stereotaxic frame (David Kopf Instruments). Holes were drilled with a micromotor handpiece drill (Foredom) after exposure of the skull. Viral injection was performed using a syringe (65458-01, Hamilton) connected to an ultra-micropump (UMP-3, World Precision Instruments). Coordinates for unilateral (right side) and bilateral injections into SPFp and PBel were: SPFp (AP, −3.1 mm; ML, 2.0 mm; DV, −3.6 mm from bregma); PBel (AP, −5.1 mm; ML, 1.35 mm; DV, −3.5 mm). Viruses were injected at a rate of 0.08 μL/min (total volume of 0.75 μL for optogenetic projection studies and 0.5 μL for all others), and syringe needles were slowly removed from the injection site 7 min after injection. To determine the inputs to $CGRP^{SPFp}$ and $CGRP^{PBel}$ neurons, 0.5 μL AAV8-hSyn-FLEX-TVA-P2A-GFP-2A-oG (3.82E+12 GC/mL; Salk Institute viral vector core) (Liu et al., 2022) was injected into the SPFp or PBel of $Calca^{Cre}$ transgenic mice. After three weeks, 0.5 μL of EnvA-ΔG-rabies-mCherry (3.95E+08 GC/mL; Salk Institute viral vector core) (Liu et al., 2022; Osakada et al., 2011) was injected into the same regions. Mice were sacrificed five days after the final injection. To silence the $CGRP^{SPFp}$ and $CGRP^{PBel}$ neurons, AAV1-DIO-GFP:TetTox (2.51E+12 GC/mL; reported validity in $Calca^{Cre}$ transgenic mice) (Carter et al., 2015; Han et al., 2015) or AAV1-DIO-EYFP (2.12E+12 GC/mL; reported validity in $Calca^{Cre}$ transgenic mice) (Bowen et al., 2020; Han et al., 2015) was injected into the SPFp (0.5 μL) or PBel (0.3 μL), respectively, of $Calca^{Cre}$ transgenic mice, and experiments were performed two weeks after injection. For Miniscope single-cell calcium imaging experiments, 0.5 μL AAV-DIO-jGCaMP8m (5E+12 GC/mL) (Liu et al., 2022; Zhang et al., 2020) was injected into the SPFp or PBel of $Calca^{Cre}$ mice and an integrated microendoscope lens (0.6 mm × 7.3 mm, Inscopix) was implanted. Coordinates for microendoscope lens implantation for SPFp and PBel were: SPFp (AP, −3.1 mm; ML, 2.0 mm; DV, −3.6 mm); PBel (AP, −4.95 mm; ML, 1.5 mm; DV, −3.6 mm).

For electrophysiological experiments, AAVDJ-EF1a-DIO-hChR2(H134R)-EYFP-WPRE-pA (4.5E+12 GC/mL) (Liu et al., 2022) was injected into the SPFp (0.5 μL) or PBel (0.3 μL) of $Calca^{Cre}$ mice. Experiments were performed two weeks after viral injection for recording SPFp and PBel neurons or four weeks after injection for recording cells in terminal regions. For optogenetics experiments, AAVDJ-EF1a-DIO-hChR2(H134R)-EYFP-WPRE-pA, AAV5-EF1a-DIO-PPO-Venus (3E+13 GC/mL) (Copits et al., 2021), AAVDJ-DIO-ArchT-GFP (1.26E+12 GC/mL) (Han et al., 2011; Liu et al., 2022) or AAV1-DIO-EYFP was injected into the SPFp (0.5 μL) or PBel (0.3 μL) of $Calca^{Cre}$ mice, and custom-made mono fiberoptic cannulae (200 um diameter, 0.22 NA) were implanted above SPFp (0.5 mm above the injection site), PBel (0.5 mm above the injection site), LA (AP, −1.8 mm; ML, 3.6 mm, DV, −4.0 mm from bregma), or CeA (AP, 1.2 mm; ML, 2.7 mm; DV, −4.2 mm from bregma). Experiments were performed two weeks after injection for cell body manipulations or four weeks for terminal manipulations.

Histology and quantification of rabies tracing experiment—Mice were intracardially perfused with 4% paraformaldehyde in PBS (phosphate buffered saline) 5 days after the rabies virus injection. Spinal cords were post-fixed at 4°C for 1 h and dehydrated with 30% sucrose at 4°C overnight. 40 μm transverse sections were obtained with a cryostat (CM, 1950; Leica) throughout the spinal cord. Spinal cord slices were directly dry mounted on superfrost plus microscope slide glasses (12-550-15, Fisher Scientific). The labeled neurons were counted manually by dividing the transverse spinal sections into four groups (cervical, thoracic, lumbar, and sacral) or different dorsal horn layers. Brains were kept in 4% PFA overnight for post-fixation and dehydrated in 30% sucrose for 1-2 days before sectioning. Frozen brains were cut into 50 μm coronal slices with a cryostat and stored in PBS before mounting. Both spinal cord and brain tissues were mounted on a slide glass with a DAPI containing mounting solution (0100-20, SouthernBiotech). Half of the slices collected throughout the brain (100 μm apart) were mounted on slide glasses and all of them were imaged with the automatic fluorescence microscope (BZ-X710, Keyence) using included imaging software (BZ-X viewer, Keyence). Red fluorescence neurons indicating the presynaptic input neurons were counted manually. Brain regions were delineated by comparing with the Allen Brain Atlas Reference Atlases.

Multi-sensory aversive stimuli experiments

Auditory stimuli: For the Miniscope single-cell calcium imaging experiment, mice were placed in a cylindrical arena (11 cm diameter with 15 cm height) with home cage bedding and habituated for 30–120 min. The experiment was controlled to have no sudden unrelated noise or visual cues. An intense sound (85 dB, 2 sec) or a control sound (70 dB, 2 sec) was played.

For the loss-of-function experiments, mice were placed inside an open field chamber and habituated for 10 min. After 1 min baseline, an intense sound (85 dB, 2 sec) was delivered three times with an inter-stimulus interval of 28 sec. Laser was shined throughout the experiment for terminal inhibition. All trials were recorded by a USB camera (DFK 33GX236, Imagine Source) attached to a computer, and freezing behavior was analyzed using video-tracking software (Ethovision XT, Noldus). Freezing behavior were monitored starting from the first stimuli to the end of the experiment and analyzed with Ethovision (“Not moving” 1.25–1.5 cm/s, for 3s samples).

Visual stimuli: For the Miniscope single-cell calcium imaging experiment, mice were placed in the same arena as the auditory experiment. The experiment was controlled to have no sudden unexpected noise or visual cues. An expanding looming stimulus (2 sec, 25-cm diameter) was delivered three times with 10 sec inter-stimulus interval with a LED screen facing the arena from above. For the loss-of-function experiment, mice were placed in a cage with bedding, positioned under the same LED screen, and habituated for 20-30 min. When mice were in the center of the cage, the expanding looming stimulus (2 sec) was delivered three times with 10 sec inter-stimulus interval. Laser was shined throughout the experiment for terminal inhibition. All trials were recorded by a USB camera (DFK 33GX236, Imagine Source) attached to a computer, and freezing behavior was analyzed using video-tracking software (Ethovision XT, Noldus). Freezing behavior were monitored starting from the first

stimuli to the end of the experiment and analyzed with Ethovision (“Not moving” 1.25–1.5 cm/s, for 3s samples).

Gustatory stimuli: For the Miniscope single-cell calcium imaging experiment, mice were placed in the same arena as used for auditory and visual stimulus experiments, but with an additional 2-cm drilled hole on the bottom. The water bottle spout was inserted into this hole, and the calcium signal was measured when mice were licking. The bottle was filled with water or quinine (0.5 mM, QU109, Spectrum Chemical).

For the loss-of-function experiment, mice were water-deprived overnight. The next day, mice were placed in a standard mouse cage with a bottle containing either water or 0.5 mM quinine inserted into the water valve slot. Mice were allowed to drink for 10 min without habituation. Laser was turned on throughout the terminal inhibition experiment. All trials were recorded by a USB camera (DFK 33GX236, Imagine Source) attached to a computer, and licking behaviors were counted manually.

Olfactory stimuli: For the Miniscope single-cell calcium imaging experiment, mice were placed in the same arena as used for gustatory stimulus experiments. A cotton swab soaked with either water- or trimethylthiazoline (TMT, 97%, 5 μL, 1G-TMT-97, BioSRQ) was inserted into the arena through the hole. Calcium signals were measured when mice smelled the cotton swab. For the loss-of-function experiment, mouse movement in a two-chamber arena (30 × 60 × 30 cm) was tracked using a USB camera (DFK 33GX236, Imagine Source) and video-tracking software (EthoVision XT 12, Noldus). Two Petri dishes with small holes were placed into each chamber–one at the corner of the left chamber, and the other at the corner of the right chamber. On day 1, mice were allowed to habituate and explore the arena for 10 min. The next day, a water-soaked cotton swab was placed in one dish, and a TMT-soaked cotton swab was placed in the other. Mice were first placed at the center of the arena and monitored for 10 min as they interacted with the two dishes. Laser was turned on throughout the terminal inhibition experiment.

Somatosensory stimuli: A threat conditioning chamber (26 × 30 × 33 cm, ENV-007CT, MED Associates) with a metal grid floor (ENV-005, MED Associates) connected to a standalone aversive electric shock stimulator (ENV-414S, MED Associates) was used for foot shock delivery. A USB camera (DFK 33GX236, Imagine Source) was connected to a computer, and video tracking software (Ethovision XT, Noldus) was used for shock delivery and behavioral analysis. The chamber was enclosed in a light- and sound-attenuating cubicle (ENV-018MD, MED Associates). The chamber was cleaned with 70% ethanol and double-distilled water after each trial.

For both Miniscope and loss-of-function experiments, mice were placed inside the chamber without habituation. After a 2 min baseline, an electric shock (2 sec, 0.6 mA) was delivered, and behavior was recorded for 2 more min. For loss-of-function experiments, freezing behavior was monitored one day before (habituation), immediately after (conditioning), and one day after the shock (post-test). For the terminal inhibition experiment, procedures were the same as for the whole-population inhibition experiment, except that the laser was turned on throughout the conditioning and post-test periods.

Cued threat conditioning: The same threat-conditioning chamber and video tracking system were used for cued threat conditioning as during somatosensory stimulus delivery. Two speakers (AX210, Dell) were placed beside the chamber to deliver auditory cues to act as conditioned stimuli (CS). The chamber was enclosed in a light- and sound-attenuating cubicle (ENV-018MD, MED Associates). The chamber was cleaned with 70% ethanol and double-distilled water between each trial. On day 1 (habituation day), mice were introduced to the chamber after connecting the optic fiber or miniature microscope. After a 2-min baseline period, CS (30 sec, 2 kHz pure tone) was delivered six times with random intervals. On day 2 (conditioning day), mice were returned to the same arena. After a 1-min baseline, mice received 5 foot-shocks (2 sec, 0.2 mA) (US) co-terminating with CS at random intervals. On day 3 (retrieval day), mice were assessed first in a context test, then a cue test after 4 h. For the context test, mice were placed into the same chamber as on the conditioning day for 3 min; for the cue test, mice were placed into a new context (a glass cylinder wrapped with a non-transparent material), and the 30-s CS was delivered alone three times (i.e., not paired with the US). For optogenetic terminal inhibition, optic fiber was connected at all times and the laser was turned on during conditioning or retrieval periods (detailed info in the Optogenetics section). Freezing behavior was analyzed by video-tracking software (EthoVision XT 12, Noldus, “Not moving” 1.25–1.5 cm/s for 3-s), which has been shown to match the manual scoring based on the characteristic rigid posture (Han et al., 2015). “BL” in the cue test indicates freezing during baseline before the first tone was delivered, and “CS+” is the average freezing during the three tones.

Miniscope single-cell calcium imaging—Calcium activity was recorded at 10 or 20 Hz and 0.4–1.2 mW/mm^2 LED power using an Inscopix nVista miniature microscope. Animals were habituated with the miniature microscope at least 3 times before the actual recording. On the testing day, over-night water-restricted animals were exposed to the following stimuli 3 times each with at least 2-min inter-trial-interval: 10 μL of 0.5 mM quinine (gustatory), cotton tip with 2 μL of 99% TMT (olfactory), 85 dB intense sound burst (auditory; 2 sec); 1 expanding looming circle (visual; 2 sec, 25-cm diameter); 0.2 mAfoot shock (somatosensory; 2 sec). All stimuli were delivered in the same miniscope-baseplate docking configuration to facilitate the registration of cells across sessions. In other words, we performed all recording sessions in one run, and during post-processing, we concatenated different videos to a single file and used it to identify cells. This design could eliminate the need for longitudinal registration of cells which would cause significant loss of cell number. The control experiments were performed during a separate session with the following stimuli delivered 3 times to water-restricted animals: 10 μL water (gustatory), cotton tip with 2 μL water (olfactory), 70 dB gentle sound (auditory; 2 sec); 1 small looming circle (visual; 2 sec, 5-cm diameter); no foot shock (somatosensory). Ethovision XT 12 was used to record behavior videos and trigger calcium activity recordings. The onset of behavioral responses was manually identified from the behavior video.

For threat conditioning recordings, the behaviors were performed following the previous “*Cued threat conditioning*” session. Separate video files were analyzed for each day without cross-registration of cells.

For data post-processing, Inscopix data processing software was used. The main steps and related parameters are listed as follows: “Preprocessing” (2x spatial downsampling, no temporal downsampling, determine crop area, fix defective pixels); “Spatial Filter” (low cut-off: 0.005 pixel^{-1}; high cut-off: 0.5 pixel^{-1}); “Motion Correct” (using the first frame as the global reference frame); “Identify Cells” (CNMFe, starting with cell diameter = 15 μm, min pixel correlation = 0.9, min pixel-to-noise ratio = 10, then adjusting parameters based on cell detection quality compared to manual identification); “Additional Tools” (deconvolve traces); “Export” (export countour map and cell traces). The output trace unit is change in fluorescence over noise (ΔF/F).

To classify cells that respond to each stimulus, we calculated z-scored calcium activity for each trial, including pre-stimulation and post-stimulation episodes. The pre-stimulation baseline period is defined as −5 to −1 sec (total 4 sec) before stimulus onset, and post-stimulation period is defined as 0 to 10 sec (total 10 sec) after stimulus onset. Since both SPFp and PBel neurons displayed baseline activity, to better visualize evoked calcium responses, we normalized the pre-stimulus baseline activity to zero by subtracting the averaged baseline activity from the whole trace. A given cell was classified as stimulus-responsive if the maximum z-score value during the post-stimulation period was larger than 2.5 in all 3 trials.

Heatmap visualization of individual neuronal activity was generated from 15-sec peri-stimulus traces (5 sec before and 10 sec after stimulus delivery) for all cells with each row indicating the same neuron across stimuli, grouped by the maximum responsive stimuli. Averaged traces of neuronal activities during the multi-sensory threat and control trials were also plotted, where representative neurons are the ones showing maximum responses to each individual stimulus. For the cued threat conditioning experiments, area under the curve (AUC) was calculated from the activities 0 to 5 sec after the stimulus onset (the stimulus refers to the tone during the habituation and cue tests, and shock during the conditioning test).

Convergent cross-mapping—We measured the network relationships between neurons using convergent cross-mapping (CCM) (Sugihara et al., 2012), a nonlinear time series embedding method based on the Takens theorem(Packard et al., 1980; Takens, 1981) and its generalized form(Deyle and Sugihara, 2011). CCM builds low-dimensional manifolds from time series and makes predictions across variables to determine causation between variables. However, in the cases where there is synchrony due to strong coupling, this causal determination cannot be made.

Here, the inputs of CCM were single-cell calcium traces pooled from multiple animals. Neurons from the same animal were highly correlated due to the stimulation protocol. Therefore, our prediction score does not measure causality within a neuron pair, but it does measure the similarity across two embedded manifolds. This non-traditional use of CCM is conceptually similar to using the prediction skills of reservoir computing models to assess the similarity between systems. This CCM measure of classification contains the information of cross-correlation, dynamic time warping, and cases for which individual local dynamical events are out of order. The main difference between CCM and the

traditional cross-correlation is that CCM correlations are in phase space and are based on topological similarities between the embedded time series. CCM correlations are measured on the manifolds of the embedded time series, taking into account the influences of latent unobserved variables that are nevertheless observable as influences on the neuronal time series. This allows CCM-based comparisons to detect similarities of dynamics that are not temporally coincident, but that occur out of sequence or with delays.

For all five sensory stimuli, we performed CCM on the peri-stimulus activity (5 sec before and 5 sec after the stimulus) of each neuron pair. The output of the CCM is a prediction score describing the similarity of manifold (neuronal dynamics and information content) within each neuron pair(Shaw, 1984). The manifold similarities were then used as inputs to compare the population recruited by each stimulus. Specifically, the prediction score matrices for each stimulus were used as inputs for hierarchical clustering using Pearson correlation as the distance metric (MATLAB “clustergram”). The clusters in the clustergram denoted the group of neurons that shared the same “broadcasters” and “receivers,” and could thus be approximated as the functional network recruited by a particular stimulus. The exact order of neurons in each clustergram (i.e., seed) was used to plot the remaining four heatmaps corresponding to the four other stimuli. We reasoned that if the same clusters could be detected in the other heatmaps, the same functional networks could be reused to respond to different stimuli. The similarity between each heatmap and its seed heatmap was quantified by their Pearson correlation coefficient for all entries. The similarities across 25 matrices were presented as a 5x5 matrix.

CCM analyses and predictions were calculated using the R package rEDM 0.7.4 (https://ha0ye.github.io/rEDM/) in the RStudio environment or with mpEDM(Watanakeesuntorn et al., 2020). These packages were run on a dual Intel Xeon Gold 6148 Server with 384GB RAM, a two-socket AMD EPYC Rome 7742 with 1TB RAM and an NVIDIA A100 40GB GPU, and an Intel Core i9 2.4 GHz MacBook Pro with 32 GB RAM. Key parameters were determined individually by lagged coordinate embedding using the simplex function implementation in rEDM to optimize predictive skill as measured by the prediction score ρ ($\Sigma obs_{(1,2,\ldots n)}/\Sigma pred_{(1,2,\ldots n)}$). Parameters included the delay τ, which calculates the characteristic timescale of the series, and the embedding dimensionality E, which estimates the number of variables driving the system. The choice of τ was informed by minimizing mutual information(Fraser and Swinney, 1986), approximately corresponding to an autocorrelation of ~0.3. To prevent data contamination, an exclusion radius larger than the smoothing window of five timesteps was applied.

Optogenetics—A 470 nm laser (LRD-0470-PFFD-00100-05, LaserGlow Tech) was used for ChR2 (4 ms pulse, 20 or 40 Hz, 8–9 mW) and PPO (10 ms pulse, 10 Hz, 8–9 mW) experiments and a 589 nm laser (LRS-0589-GFM-00050-05, continuous, 6-7 mW) was used for ArchT experiments. Optic fibers were bilaterally connected to pre-implanted optic ferrules on the mice.

Real-time place aversion (RTPA): A two-chamber arena (30 × 60 × 30) was used for the RTPA test. Behavior was tracked with a USB camera (DFK 33GX236, Imagine Source) using video-tracking software (EthoVision XT 12, Noldus). After connecting the optic fiber,

mice were placed in one side of the chamber. No stimulation was given for a 10-min baseline period. One side of the chamber was then pseudorandomly selected, and the mouse was photostimulated (20 Hz for cell body stimulation, and 40 Hz for terminal stimulation, 8–9 mW) for as long as it stayed in that chamber. The test ended 20 min after initiation of the photostimulation phase. The stimulated chamber was counterbalanced between animals. Mice showing over 15% preference to one side during baseline were excluded. The first 10 min (baseline) was used for laser "OFF" and the last 10 min (20–30 min) during the photostimulation phase was laser "ON". Time spent in the stimulated side of the chamber (%) was used for RTPA data presentation.

Auditory cue dependent optogenetic conditioning: The experimental paradigms for auditory cue-dependent optogenetic conditioning were the same as those described in the "Cued threat conditioning" section above, except that 10-s photostimulation (20 Hz frequency for cell body and 40 Hz for terminal stimulation, 8–9 mW intensity) was used as the US instead of foot shock. The 10-s photostimulation is an artificial protocol that was used to induce threat memory in a previous study (Han et al., 2015). It does not mimic the endogenous activity.

Terminal inhibition during multi-sensory aversive stimuli: Laser (10 Hz 470 nm for PPO and continuous 589 nm for ArchT) was kept on during the whole experiment to allow thorough inhibition during the stimuli and avoid rebound activity during the conditioning trial.

Terminal inhibition during cued threat conditioning: The experimental paradigms for terminal inhibition during cued threat conditioning were the same as those described in the "Cued threat conditioning" section above, except that terminal photoinhibition was performed during conditioning or retrieval period. To inhibit during the conditioning period, laser (10 Hz 470 nm for PPO and continuous 589 nm for ArchT) was turned on from 10s after the start of the first tone until the end of the conditioning trial. This was to allow thorough inhibition during the shock episode and avoid rebound activity during the conditioning trial. To inhibit during the retrieval period, laser was kept on during the whole context and cue test.

Preparation of acute brain slices and electrophysiology with optogenetics: *Calca*^{Cre} mice injected with AAV-DIO-ChR2-EYFP in the SPFp or PBel were anesthetized with isoflurane and perfused via the vascular system using ice-cold cutting solution (110.0 mM choline chloride, 25.0 mM $NaHCO_3$, 1.25 mM NaH_2PO_4, 2.5 mM KCl, 0.5 mM $CaCl_2$, 7.0 mM $MgCl_2$, 25.0 mM glucose, 5.0 mM ascorbic acid and 3.0 mM pyruvic acid, bubbled with 95% O_2 and 5% CO_2). After decapitation, brains were quickly removed and chilled in an ice-cold cutting solution. Coronal slices containing the pIC or the amygdaloid complex (300 μm) were cut by using a Leica VT 1200S Vibratome (Leica Biosystems), and subsequently transferred to a storage chamber containing artificial cerebrospinal fluid (aCSF; 124 mM NaCl, 2.5 mM KCl, 26.2 mM $NaHCO_3$, 1.2 mM NaH_2PO_4, 13 mM glucose, 2 mM $MgSO_4$ and 2 mM $CaCl_2$, at 32°C, pH 7.4, bubbled with 95% O_2 and 5% CO_2). After at least 30 min recovery time, slices were maintained at room

temperature (22–24°C) for at least 60 min before use. Slices were transferred into the recording chamber, perfused with aCSF (flow rate ~2 mL/min). The temperature of aCSF was held constant at 32°C by TC-324C temperature controller (Warner Instruments). The neurons were visualized under trans-illumination by far-red microscope (Scientifica) and pyramidal neurons (LA, pIC) or medium spiny neurons (AStr) were patched based on the morphology. Recording glass electrode (3.0–5.0 Mom) was back filled with internal solution: $CsMeSO_3$ 130 mM, CsCl 5 mM, HEPES 10 mM, $MgCl_2$ 2.5 mM, EGTA 0.6 mM, Sodium phosphocreatine 10 mM, Na_2ATP 4 mM and Na_3GTP 0.4 mM, pH 7.23, 285 Osm). Whole-cell patch clamp was performed with Multiclamp 700B amplifiers (Molecular Devices). Signals were digitized at 10 kHz with Digidata 1550B (Molecular Devices). 2–5 ms pulse of 470 nm LED light (TTL from Clampex to Cool Led pE-300) was illuminated through 40X NA 0.8 objective lens at 0.1 Hz to evoke optogenetically evoked postsynaptic current. The internal solution was calculated to make chloride reversal potential equal −70 mV. EPSCs were recorded at −70 mV, and IPSCs were recorded at 0 mV. CNQX (10 μM) was perfused to verify the glutamatergic synapse. EPSCs and IPSCs were analyzed using pCLAMP 10 software (Molecular Devices). Latency was defined as the time from the initiation of the 470 nm LED light to the 5% of EPSC or IPSC peak amplitude.

Imaging—The images were taken with an automatic fluorescence microscope (BZ-X710, Keyence) using included imaging software (BZ-X viewer, Keyence) or with a scanning confocal microscope (FV 1000, Olympus) using with Fluoview software (Olympus). For quantification purposes, images were processed with the same gain, offset, and exposure time. Cell counting for retrograde tracing was done manually.

QUANTIFICATION AND STATISTICAL ANALYSIS

Quantifications of miniscope single-cell imaging, monosynaptic rabies tracing, behavioral tests, and electrophysiology are described in the corresponding sections of text and methods. All data are presented as mean ± SEM and were analyzed using Student's t-test, one-way ANOVA with Tukey's post hoc comparison, and two-way ANOVA with Sidak's post hoc comparison when the they passed the Shapiro-Wilk normality test. If not ($p < 0.05$), data were analyzed with MannWhitney test and Kruskal-Wallis one-way ANOVA with Dunn's multiple comparisons test. All statistical analyses were done using Prism 6 (GraphPad Software) and Sigmaplot 14.0 (Systat Software Inc.). NS $p > 0.05$, *$p < 0.05$, **$p < 0.01$, ***$p < 0.001$. Full details of statistical tests in individual figures are described in the figure legend and Table S5.

Supplementary Material

Refer to Web version on PubMed Central for supplementary material.

ACKNOWLEDGMENTS

The authors thank D. O'Keefe for stylistic editing of the manuscript. S.H. is supported by 1R01MH116203 from NIMH and the Bridge to Independence award from the Simons Foundation Autism Research Initiative (SFARI #388708). S.L. is supported by the Salk Women & Science Special Award, the Mary K. Chapman Foundation, and the Jesse & Caryl Philips Foundation. M.R.B. and B.C. were supported by 1R01MH111520, and M.R.B. also by R01MH112355.

REFERENCES

Ashina M (2020). Migraine. N. Engl. J. Med 383, 1866–1876. [PubMed: 33211930]

Ashina H, Iljazi A,Al-Khazali HM, Eigenbrodt AK, Larsen EL,Andersen AM, Hansen KJ, Bräuner KB, Mørch-Jessen T, Chaudhry B, et al. (2020). Efficacy, tolerability, and safety of erenumab for the preventive treatment of persistent post-traumatic headache attributed to mild traumatic brain injury: an open-label study. J. Headache Pain 21, 62. [PubMed: 32493206]

Bach DR, Hurlemann R, and Dolan RJ (2015). Impaired threat prioritisation after selective bilateral amygdala lesions. Cortex 63, 206–213. [PubMed: 25282058]

Barsy B, Kocsis K, Magyar A, Babiczky Á, Szabó M, Veres JM, Hillier D, Ulbert I, Yizhar O, and Mátyás F (2020). Associative and plastic thalamic signaling to the lateral amygdala controls fear behavior. Nat. Neurosci 23, 625–637. [PubMed: 32284608]

Blanchard DC, and Blanchard RJ (1972). Innate and conditioned reactions to threat in rats with amygdaloid lesions. J. Comp. Physiol. Psychol 81, 281–290. [PubMed: 5084445]

Bowen AJ, Chen JY, Huang YW, Baertsch NA, Park S, and Palmiter RD (2020). Dissociable control of unconditioned responses and associative fear learning by parabrachial CGRP neurons. Elife 9, e59799. [PubMed: 32856589]

Campos CA, Bowen AJ, Roman CW, and Palmiter RD (2018). Encoding of danger by parabrachial CGRP neurons. Nature 555, 617–622. [PubMed: 29562230]

Canteras NS (2002). The medial hypothalamic defensive system: hodological organization and functional implications. Pharmacol. Biochem. Behav 71, 481–491. [PubMed: 11830182]

Carter ME, Soden ME, Zweifel LS, and Palmiter RD (2013). Genetic identification of a neural circuit that suppresses appetite. Nature 503, 111–114. [PubMed: 24121436]

Carter ME, Han S, and Palmiter RD (2015). Parabrachial calcitonin gene-related peptide neurons mediate conditioned taste aversion. J. Neurosci 35, 4582–4586. [PubMed: 25788675]

Chen JY, Campos CA, Jarvie BC, and Palmiter RD (2018). Parabrachial CGRP neurons establish and sustain aversive taste memories. Neuron 100, 891–899.e5. [PubMed: 30344042]

Chiang MC, Nguyen EK, Canto-Bustos M, Papale AE, Oswald A-MM, and Ross SE (2020). Divergent neural pathways emanating from the lateral parabrachial nucleus mediate distinct components of the pain response. Neuron 106, 927–939.e5. [PubMed: 32289251]

Choi S, Hachisuka J, and Ginty D (2020). Parallel ascending spinal pathways for affective touch and pain. Nature 587, 258–263. [PubMed: 33116307]

Comeras LB, Herzog H, and Tasan RO (2019). Neuropeptides at the crossroad of fear and hunger: a special focus on neuropeptide Y. Ann. N. Y. Acad. Sci 1455, 59–80. [PubMed: 31271235]

Coolen LM, Veening JG, Wells AB, and Shipley MT (2003a). Afferent connections of the parvocellular subparafascicular thalamic nucleus in the rat: evidence for functional subdivisions. J. Comp. Neurol 463, 132–156. [PubMed: 12815752]

Coolen LM, Veening JG, Petersen DW, and Shipley MT (2003b). Parvocellular subparafascicular thalamic nucleus in the rat: anatomical and functional compartmentalization. J. Comp. Neurol 463, 117–131.

Copits BA, Gowrishankar R, O'Neill PR, Li J-N, Girven KS, Yoo JJ, Meshik X, Parker KE, Spangler SM, Elerding AJ, et al. (2021). A photoswitchable GPCR-based opsin for presynaptic inhibition. Neuron 109, 1791–1809.e11. [PubMed: 33979635]

Craig AD, Bushnell MC, Zhang E-T, and Blomqvist A (1994).Athalamic nucleus specific for pain and temperature sensation. Nature 372, 770–773. [PubMed: 7695716]

Craig AD, Chen K, Bandy D, and Reiman EM (2000). Thermosensory activation of insular cortex. Nat. Neurosci 3, 184–190. [PubMed: 10649575]

Dal Monte O, Costa VD, Noble PL, Murray EA, and Averbeck BB (2015). Amygdala lesions in rhesus macaques decrease attention to threat. Nat. Commun 6, 10161. [PubMed: 26658670]

Demarquay G, and Mauguière F (2016). Central nervous system underpinnings of sensory hypersensitivity in migraine: insights from neuroimaging and electrophysiological studies. Headache 56, 1418–1438. [PubMed: 26350583]

Deyle ER, and Sugihara G (2011). Generalized theorems for nonlinear state space reconstruction. PLoS One 6, e18295. [PubMed: 21483839]

D'Hanis W, Linke R, and Yilmazer-Hanke D.m. (2007). Topography of thalamic and parabrachial calcitonin gene-related peptide (CGRP) immunoreactive neurons projecting to subnuclei of the amygdala and extended amygdala. J. Comp. Neurol 505, 268–291. [PubMed: 17879271]

Dobolyi A, Irwin S, Makara G, Usdin TB, and Palkovits M (2005). Calcitonin gene-related peptide-containing pathways in the rat forebrain. J. Comp. Neurol 489, 92–119. [PubMed: 15977170]

Feinstein JS, Adolphs R, Damasio A, and Tranel D (2011). The human amygdala and the induction and experience of fear. Curr. Biol 21, 34–38. [PubMed: 21167712]

Ferreira A, Pereira M, Agrati D, Uriarte N, and Fernández-Guasti A (2002). Role of maternal behavior on aggression, fear and anxiety. Physiol. Behav 77, 197–204. [PubMed: 12419395]

Fraser AM, and Swinney HL (1986). Independent coordinates for strange attractors from mutual information. Phys. Rev. A Gen. Phys 33, 1134–1140. [PubMed: 9896728]

Fu J-Y, Yu X-D, Zhu Y, Xie S-Z, Tang M-Y, Yu B, and Li X-M (2020). Whole-brain map of long-range monosynaptic inputs to different cell types in the amygdala of the mouse. Neurosci. Bull 36, 1381–1394. [PubMed: 32691225]

Garcia-Diaz DE, Jimenez-Montufar LL, Guevara-Aguilar R, Wayner MJ, and Armstrong DL (1988). Olfactory and visceral projections to the nucleus of the solitary tract. Physiol. Behav 44, 619–624. [PubMed: 3237848]

Gauriau C, and Bernard J-F (2004). Posterior triangular thalamic neurons convey nociceptive messages to the secondary somatosensory and insular cortices in the rat. J. Neurosci 24, 752–761. [PubMed: 14736861]

Gross CT, and Canteras NS (2012). The many paths to fear. Nat. Rev. Neurosci 13, 651–658. [PubMed: 22850830]

Han S, Soleiman MT, Soden ME, Zweifel LS, and Palmiter RD (2015). Elucidating an affective pain circuit that creates a threat memory. Cell 162, 363–374. [PubMed: 26186190]

Han X, Chow BY, Zhou H, Klapoetke NC, Chuong A, Rajimehr R, Yang A, Baratta MV, Winkle J, Desimone R, and Boyden ES (2011). A high-light sensitivity optical neural silencer: development and application to optogenetic control of non-human primate cortex. Front. Syst. Neurosci 5, 18. [PubMed: 21811444]

Harriott AM, and Schwedt TJ (2014). Migraine is associated with altered processing of sensory stimuli. Curr. Pain Headache Rep 18, 458. [PubMed: 25245197]

Harte SE, Ichesco E, Hampson JP, Peltier SJ, Schmidt-Wilcke T, Clauw DJ, and Harris RE (2016). Pharmacologic attenuation of cross-modal sensory augmentation within the chronic pain insula. Pain 157, 1933–1945. [PubMed: 27101425]

Janak PH, and Tye KM (2015). From circuits to behaviour in the amygdala. Nature 517, 284–292. [PubMed: 25592533]

Jarvie BC, Chen JY, King HO, and Palmiter RD (2021). Satb2 neurons in the parabrachial nucleus mediate taste perception. Nat. Commun 12, 224. [PubMed: 33431851]

Kim JJ, and Fanselow MS (1992). Modality-specific retrograde amnesia of fear. Science 256, 675–677. [PubMed: 1585183]

Kim EJ, Jacobs MW, Ito-Cole T, and Callaway EM (2016). Improved monosynaptic neural circuit tracing using engineered rabies virus glycoproteins. Cell Rep. 15, 692–699. [PubMed: 27149846]

Kim J, Zhang X, Muralidhar S, LeBlanc SA, and Tonegawa S (2017). Basolateral to central amygdala neural circuits for appetitive behaviors. Neuron 93, 1464–1479.e5. [PubMed: 28334609]

Kocorowski LH, and Helmstetter FJ (2001). Calcitonin gene-related peptide released within the amygdala is involved in pavlovian auditory fear conditioning. Neurobiol. Learn. Mem 75, 149–163. [PubMed: 11222057]

Kruger L, Sternini C, Brecha NC, and Mantyh PW (1988). Distribution of calcitonin gene-related peptide immunoreactivity in relation to the rat central somatosensory projection. J. Comp. Neurol 273, 149–162. [PubMed: 3047185]

Kunwar PS, Zelikowsky M, Remedios R, Cai H, Yilmaz M, Meister M, and Anderson DJ (2015). Ventromedial hypothalamic neurons control a defensive emotion state. Elife 4, e06633.

de Lacalle S, and Saper CB (2000). Calcitonin gene-related peptide-like immunoreactivity marks putative visceral sensory pathways in human brain. Neuroscience 100, 115–130. [PubMed: 10996463]

LeDoux J (2012). Rethinking the emotional brain. Neuron 73, 653–676. [PubMed: 22365542]

LeDoux JE (2000). Emotion circuits in the brain. Annu. Rev. Neurosci 23, 155–184. [PubMed: 10845062]

LeDoux JE, Ruggiero DA, and Reis DJ (1985). Projections to the subcortical forebrain from anatomically defined regions of the medial geniculate body in the rat. J. Comp. Neurol 242, 182–213. [PubMed: 4086664]

Li Z, Wei J-X, Zhang G-W, Huang JJ, Zingg B, Wang X, Tao HW, and Zhang LI (2021). Corticostriatal control of defense behavior in mice induced by auditory looming cues. Nat. Commun 12, 1040. [PubMed: 33589613]

Liu S, Ye M, Pao GM, Song SM, Jhang J, Jiang H, Kim J-H, Kang SJ, Kim D-I, and Han S (2022). Divergent brainstem opioidergic pathways that coordinate breathing with pain and emotions. Neuron 110, 857–873.e9. [PubMed: 34921781]

López-Solà M, Woo C-W, Pujol J, Deus J, Harrison BJ, Monfort J, and Wager TD (2017). Towards a neurophysiological signature for fibromyalgia. Pain 158, 34–47. [PubMed: 27583567]

Nagy V, Bozdagi O, Matynia A, Balcerzyk M, Okulski P, Dzwonek J, Costa RM, Silva AJ, Kaczmarek L, and Huntley GW (2006). Matrix metalloproteinase-9 is required for hippocampal late-phase long-term potentiation and memory. J. Neurosci 26, 1923–1934. [PubMed: 16481424]

Nakamura K, and Morrison SF (2008). A thermosensory pathway that controls body temperature. Nat. Neurosci 11, 62–71. [PubMed: 18084288]

Nelson KB, Grether JK, Croen LA, Dambrosia JM, Dickens BF, Jelliffe LL, Hansen RL, and Phillips TM (2001). Neuropeptides and neurotrophins in neonatal blood of children with autism or mental retardation. Ann. Neurol 49, 597–606. [PubMed: 11357950]

Osakada F, Mori T, Cetin AH, Marshel JH, Virgen B, and Callaway EM (2011). New rabies virus variants for monitoring and manipulating activity and gene expression in defined neural circuits. Neuron 71, 617–631. [PubMed: 21867879]

Packard NH, Crutchfield JP, Farmer JD, and Shaw RS (1980). Geometry from a time series. Phys. Rev. Lett 45, 712–716.

Palmiter RD (2018). The Parabrachial nucleus: CGRP neurons function as a general alarm. Trends Neurosci. 41, 280–293. [PubMed: 29703377]

Price DD (2002). Central neural mechanisms that interrelate sensory and affective dimensions of pain. Mol. Interv 2, 392–403.e9. [PubMed: 14993415]

Ren W, and Neugebauer V (2010). Pain-related increase of excitatory transmission and decrease of inhibitory transmission in the central nucleus of the amygdala are mediated by mGluR1. Mol. Pain 6, 93. [PubMed: 21162731]

Rizvi TA, Ennis M, Behbehani MM, and Shipley MT (1991). Connections between the central nucleus of the amygdala and the midbrain periaqueductal gray: topography and reciprocity. J. Comp. Neurol 303, 121–131. [PubMed: 1706363]

Rosen JB, Asok A, and Chakraborty T (2015). The smell of fear: innate threat of 2, 5-dihydro-2, 4, 5-trimethylthiazoline, a single molecule component of a predator odor. Front. Neurosci 9, 292. [PubMed: 26379483]

Russell FA, King R, Smillie S-J, Kodji X, and Brain SD (2014). Calcitonin gene-related peptide: physiology and pathophysiology. Physiol. Rev 94, 1099–1142. [PubMed: 25287861]

Russo AF (2015). Calcitonin Gene-Related Peptide (CGRP): a new target for migraine. Annu. Rev. Pharmacol. Toxicol 55, 533–552. [PubMed: 25340934]

Salay LD, Ishiko N, and Huberman AD (2018). A midline thalamic circuit determines reactions to visual threat. Nature 557, 183–189. [PubMed: 29720647]

Sato M, Ito M, Nagase M, Sugimura YK, Takahashi Y, Watabe AM, and Kato F (2015). The lateral parabrachial nucleus is actively involved in the acquisition of fear memory in mice. Mol. Brain 8, 22. [PubMed: 25888401]

Scott SK, Young AW, Calder AJ, Hellawell DJ, Aggleton JP, and Johnson M (1997). Impaired auditory recognition of fear and anger following bilateral amygdala lesions. Nature 385, 254–257. [PubMed: 9000073]

Shaw R (1984). The Dripping Faucet as a Model Chaotic System (Aerial Press).

Shinohara K, Watabe AM, Nagase M, Okutsu Y, Takahashi Y, Kurihara H, and Kato F (2017). Essential role of endogenous calcitonin gene-related peptide in pain-associated plasticity in the central amygdala. Eur. J. Neurosci 46, 2149–2160. [PubMed: 28833700]

Silva BA, Mattucci C, Krzywkowski P, Murana E, Illarionova A, Grinevich V, Canteras NS, Ragozzino D, and Gross CT (2013). Independent hypothalamic circuits for social and predator fear. Nat. Neurosci 16, 1731–1733. [PubMed: 24212674]

Silva BA, Gross CT, and Gräff J (2016). The neural circuits of innate fear: detection, integration, action, and memorization. Learn. Mem 23, 544–555. [PubMed: 27634145]

Simons LE, Moulton EA, Linnman C, Carpino E, Becerra L, and Borsook D (2014). The human amygdala and pain: evidence from neuroimaging. Hum. Brain Mapp 35, 527–538. [PubMed: 23097300]

Sugihara G, May R, Ye H, Hsieh C. -h., Deyle E, Fogarty M, and Munch S (2012). Detecting causality in complex ecosystems. Science 338, 496–500. [PubMed: 22997134]

Takens F (1981). Detecting strange attractors in turbulence. In Dynamical Systems and Turbulence, Warwick 1980, Rand D and Young L-S, eds. (Springer), pp. 366–381.

Tong WH, Abdulai-Saiku S, and Vyas A (2020). Medial amygdala arginine vasopressin neurons regulate innate aversion to cat odors in male mice. Neuroendocrinology 111, 505–520. [PubMed: 32447337]

Usunoff KG, Itzev DE, Rolfs A, Schmitt O, and Wree A (2006). Brain stem afferent connections of the amygdala in the rat with special references to a projection from the parabigeminal nucleus: a fluorescent retrograde tracing study. Anat. Embryol 211, 475–496.

Veinante P, Yalcin I, and Barrot M (2013). The amygdala between sensation and affect: a role in pain. J. Mol. Psychiatry 1, 9. [PubMed: 25408902]

Viviani D, Charlet A, van den Burg E, Robinet C, Hurni N, Abatis M, Magara F, and Stoop R (2011). Oxytocin selectively gates fear responses through distinct outputs from the Central Amygdala. Science 333, 104–107. [PubMed: 21719680]

Wang L, Gillis-Smith S, Peng Y, Zhang J, Chen X, Salzman CD, Ryba NJP, and Zuker CS (2018). The coding of valence and identity in the mammalian taste system. Nature 558, 127–131. [PubMed: 29849148]

Watanakeesuntorn W, Takahashi K, Ichikawa K, Park J, Sugihara G, Takano R, Haga J, and Pao GM (2020). Massively parallel causal inference of whole brain dynamics at single neuron resolution. In 2020 IEEE 26th International Conference on Parallel and Distributed Systems (ICPADS), pp. 196–205.

Wei P, Liu N, Zhang Z, Liu X, Tang Y, He X, Wu B, Zhou Z, Liu Y, Li J, et al. (2015). Processing of visually evoked innate fear by a non-canonical thalamic pathway. Nat. Commun 6, 8228. [PubMed: 26293832]

Yasui Y, Saper CB, and Cechetto DF (1991). Calcitonin gene-related peptide (CGRP) immunoreactive projections from the thalamus to the striatum and amygdala in the rat. J. Comp. Neurol 308, 293–310. [PubMed: 1890240]

Yasui Y, Nakano K, and Mizuno N (1992). Descending projections from the subparafascicular thalamic nucleus to the lower brain stem in the rat. Exp. Brain Res 90, 508–518. [PubMed: 1385199]

Yu L-C, Hou J-F, Fu F-H, and Zhang Y-X (2009). Roles of calcitonin gene-related peptide and its receptors in pain-related behavioral responses in the central nervous system. Neurosci. Biobehav. Rev 33, 1185–1191. [PubMed: 19747596]

Zhang G-W, Sun W-J, Zingg B, Shen L, He J, Xiong Y, Tao HW, and Zhang LI (2018). A non-canonical reticular-limbic central auditory pathway via medial septum contributes to fear conditioning. Neuron 97, 406–417.e4. [PubMed: 29290554]

Zhang Y, Rózsa M, Bushey D, Zheng J, Reep D, Liang Y, Broussard GJ, Tsang A, Tsegaye G, Patel R, et al. (2020). jGCaMP8 Fast Genetically Encoded Calcium Indicators.

Online resource (Janelia Research Campus). https://janelia.figshare.com/articles/online_resource/jGCaMP8_Fast_Genetically_Encoded_Calcium_Indicators/13148243.

Zhou Z, Liu X, Chen S, Zhang Z, Liu Y, Montardy Q, Tang Y, Wei P, Liu N, Li L, et al. (2019). A VTA GABAergic neural circuit mediates visually evoked innate defensive responses. Neuron 103, 473–488.e6. [PubMed: 31202540]

Highlights

- $CGRP^{SPFp}$ and $CGRP^{PBel}$ neurons mediate multi-sensory innate threat perception
- These neurons send aversive information to different subregions of the amygdala
- $CGRP^{SPFp \rightarrow LA}$ and $CGRP^{PBel \rightarrow CeA}$ circuits are crucial for aversive memory formation

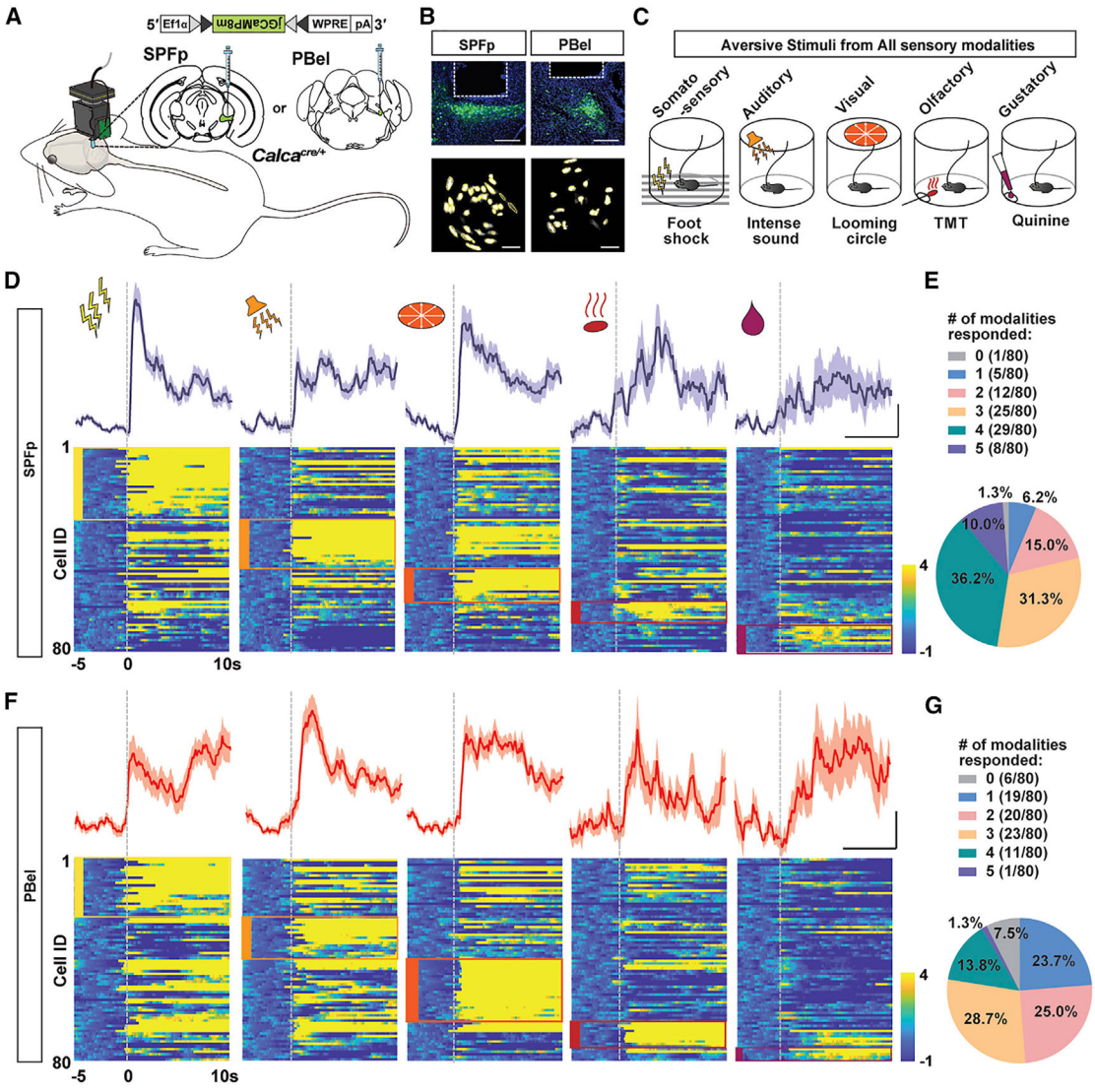

Figure 1. Individual CGRP^{SPFp} and CGRP^{PBel} neurons respond to multi-modal innate threat stimuli

(A–C) Schematic (A), histological verification (B), and behavioral design (C) of single-cell calcium imaging of CGRP^{SPFp} and CGRP^{PBel} neurons with miniature microscope during innate threat stimuli presentation. Scale bars in (B), 200 μm (top) and 100 μm (bottom).

(D and F) Bottom: heatmaps of *Z*-scored CGRP^{SPFp} (D) and CGRP^{PBel} (F) single-cell activity aligned at the onset of stimulus delivery (dotted line) across five different modalities. Clusters of neurons that preferentially respond to certain stimulus types are labeled with boxes of corresponding color. Top: averaged activity from neurons that best respond to each sensory modality. Scale: 5 s/2 *Z*-scored Δ*F*/*F*. n = 80 cells/3 mice in each group.

(E and G) Percentage of CGRP^{SPFp} (E) and CGRP^{PBel} (G) neurons that respond to different numbers of modalities. Data are presented as mean ± SEM.

See also Figures S1 and S2.

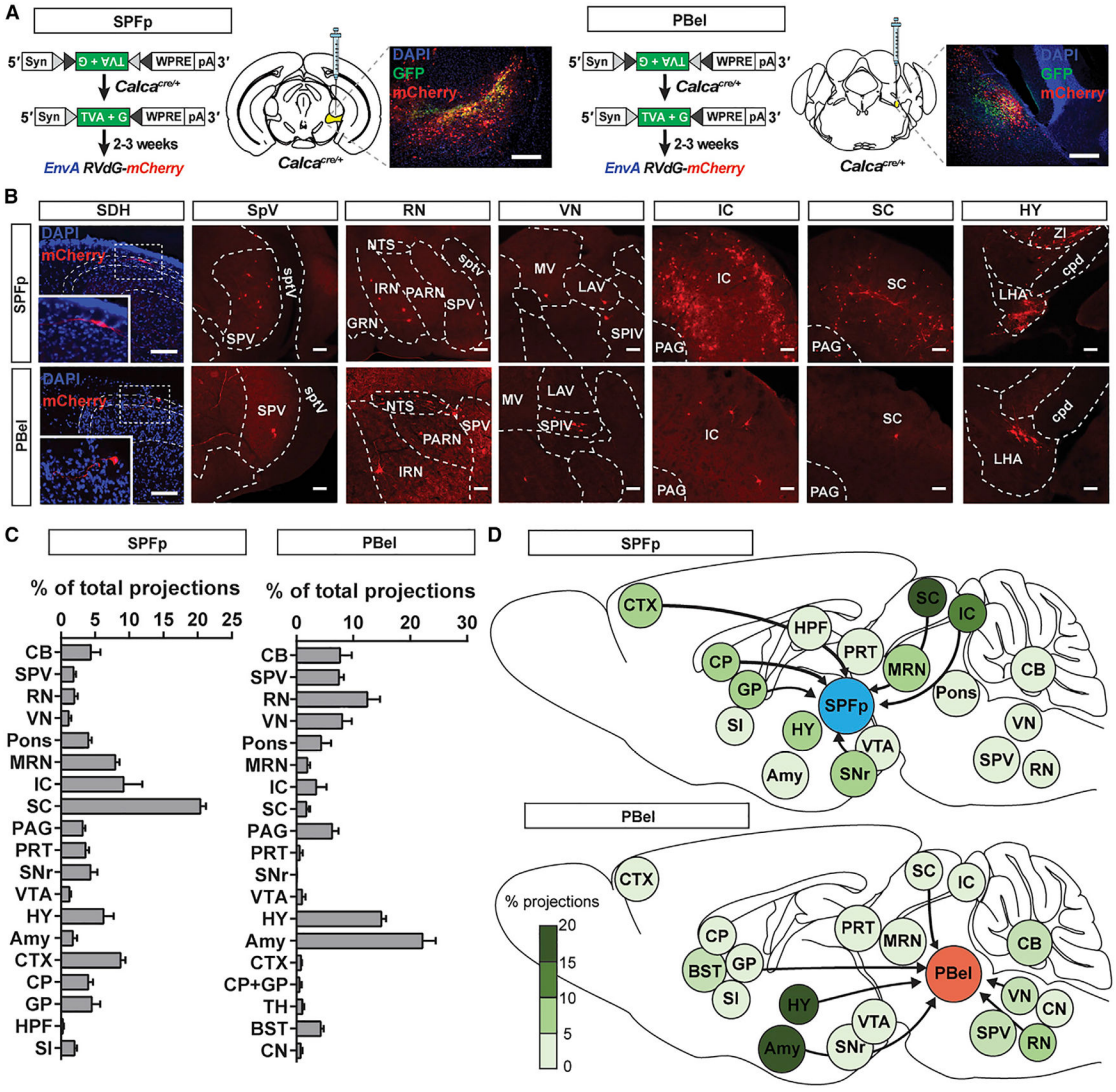

Figure 2. Retrograde tracing from CGRP^{SPFp} and CGRP^{PBel} neurons

(A) Schematic of monosynaptic retrograde rabies tracing experiment and example histology image of the CGRP^{SPFp} (left) and CGRP^{PBel} (right) starter cells. Scale bars, 200 μm.

(B) Example images of spinal dorsal horn and brain regions that send inputs to CGRP^{SPFp} (top) and CGRP^{PBel} (bottom) neurons. Scale bars, 100 μm.

(C) Percentage of total projections from each brain region to CGRP^{SPFp} (left) and CGRP^{PBel} (right) neurons. n = 5 (CGRP^{SPFp}), n = 6 mice (CGRP^{PBel}).

(D) Diagrams of brain-wide inputs to CGRP^{SPFp} (top) and CGRP^{PBel} (bottom) neurons and their relative percentages.

SDH, spinal dorsal horn; CB, cerebellum including interposed nucleus (IP), arbor vitae (arb); SPV, trigeminal spinal nucleus; RN, reticular nucleus including the nucleus tractus solitarius (NTS), intermediate reticular nucleus (IRN), parvicellular reticular nucleus (PARN), gigantocellular reticular nucleus (GRN); VN, vestibular nucleus including medial vestibular nucleus (MV), lateral vestibular nucleus (LAV), spinal vestibular nucleus (SPIV); Pons including the nucleus of the lateral lemniscus, pontine central gray, parabrachial

nucleus, pontine reticular nucleus (PRN); MRN, midbrain reticular nucleus; IC, inferior colliculus; SC, superior colliculus; PAG, periaqueductal gray; PRT, pretectal region including anterior pretectal nucleus (APN), medial pretectal area (MPT), nucleus of the posterior commissure (NPC), olivary pretectal nucleus (OP); SNr, substantia nigra; VTA, ventral tegmental area; HY, hypothalamus including lateral hypothalamus (LHA), zona incerta (ZI); Amy, amygdala; CTX, cortex; CP, striatum; GP, globus pallidus; HPF, hippocampus; TH, thalamus; BST, bed nuclei of the stria terminalis; SI, substantia innominata; sptv, spinal tract of the trigeminal nerve; cpd, cerebral peduncle. Data are presented as mean ± SEM. See also Figure S3; Tables S2 and S3.

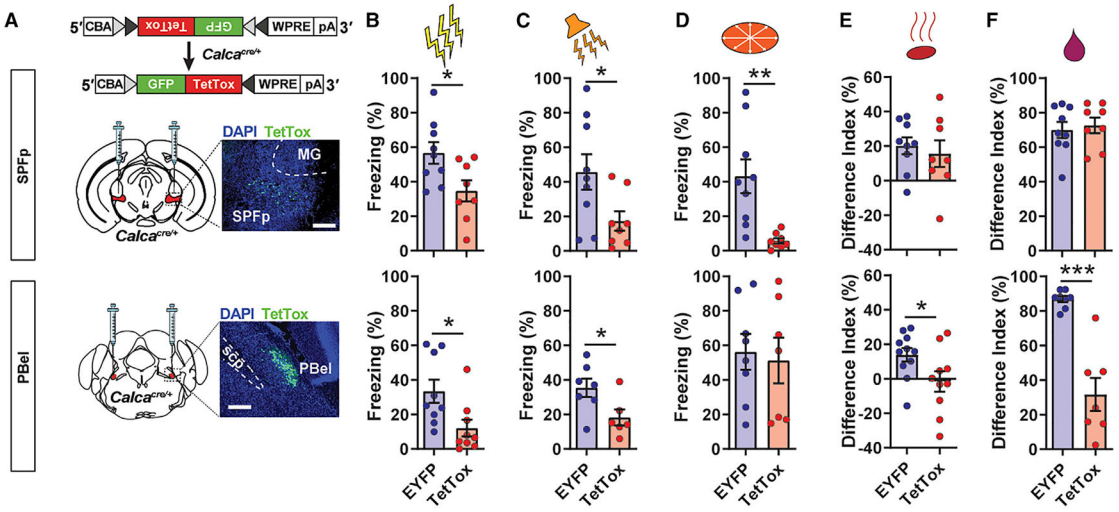

Figure 3. CGRP^{SPFp} or CGRP^{PBel} neurons are required for perception of innate threats of various modalities

(A) Schematic and histological verification of TetTox expression in the CGRP^{SPFp} (top) or CGRP^{PBel} neurons (bottom). Scale bars, 200 μm.

(B) Mice expressing TetTox in CGRP^{SPFp} and CGRP^{PBel} neurons displayed less freezing in response to electric foot shock (2 s, 0.6 mA) than EYFP controls. SPFp: n = 9 (EYFP), n = 8 (TetTox) mice; PBel: n = 9 (EYFP), n = 9 (TetTox) mice.

(C) Mice expressing TetTox in CGRP^{SPFp} and CGRP^{PBel} neurons displayed less freezing in response to intense sound (85 dB) than controls. SPFp: n = 9 (EYFP), n = 8 (TetTox) mice; PBel: n = 7 (EYFP), n = 6 (TetTox) mice.

(D) Mice expressing TetTox in CGRP^{SPFp} neurons, but not CGRP^{PBel} neurons, displayed less freezing in response to looming stimuli than controls. SPFp: n = 9 (EYFP), n = 8 (TetTox) mice; PBel: n = 8 (EYFP), n = 7 (TetTox) mice.

(E) The CGRP^{PBel} TetTox group, but not the CGRP^{SPFp} TetTox group, demonstrated reduced avoidance behaviors toward TMT in a two-chamber choice test. SPFp: n = 9 (EYFP), n = 8 (TetTox) mice; PBel: n = 11 (EYFP), n = 10 (TetTox) mice.

(F) Preference for water over quinine in a two-bottle choice test was intact in the CGRP^{SPFp} TetTox group and greatly reduced in the CGRP^{PBel} TetTox group. SPFp: n = 9 (EYFP), n = 8 (TetTox) mice; PBel: n = 8 (EYFP), n = 7 (TetTox) mice.

Data are presented as mean ± SEM. Statistical analyses were performed using two-tailed unpaired t tests (B–F); see also Table S5 for statistical details. *p < 0.05, **p < 0.01, ***p < 0.001.

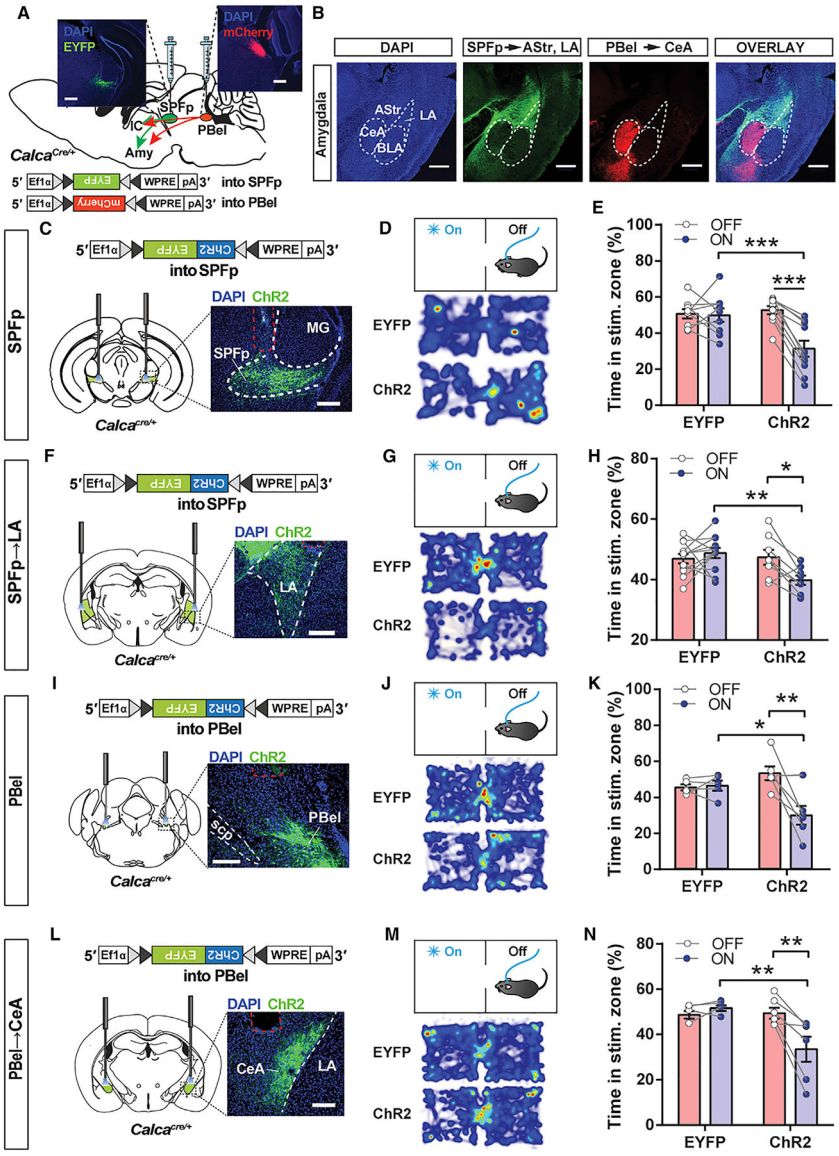

Figure 4. CGRP^{SPFp} and CGRP^{PBel} neurons relay negative valence to the LA and CeA

(A) Schematic and representative images of Cre-dependent expression of EYFP in the SPFp and mCherry in the PBel of a *Calca*^{Cre} mouse. Scale bars, 200 μm.

(B) Axonal projections from the CGRP^{SPFp} and CGRP^{PBel} neurons in the amygdala are mutually exclusive. Scale bars, 500 μm.

(Cand D) Viral expression schematic, histological verification (C), and heatmap (D) of real-time place aversion (RTPA) experiment with CGRP^{SPFp} cell-body photostimulation. Scale bars, 200 μm.

(E) ChR2-expressing mice, but not EYFP controls, avoided the chamber paired with CGRP^{SPFp} cell-body photostimulation. n = 9 (EYFP), n = 10 (ChR2) mice. Data indicate the percentage of time spent in the photostimulated zone during the baseline (OFF, 0–10 min) and the last 10 min of photostimulation period (ON, 20–30 min).

(F and G) Viral expression schematic, histological verification (F), and heatmap (G) of $CGRP^{SPFp \rightarrow LA}$ terminal photostimulation for RTPA experiment. Scale bars, 200 μm.
(H) ChR2-expressing mice, but not EYFP controls, avoided the chamber paired with $CGRP^{SPFp \rightarrow LA}$ terminal photostimulation. n = 12 (EYFP), n = 8 (ChR2) mice. (I and J) Viral expression schematic, histological verification (I), and heatmap of RTPA experiment (J) with $CGRP^{PBel}$ cell-body photostimulation. Scale bars, 200 μm.
(K) ChR2-expressing mice, but not EYFP controls, avoided the chamber paired with $CGRP^{PBel}$ cell-body photostimulation. n = 5 (EYFP), n = 6 (ChR2) mice.
(L and M) Viral expression schematic, histological verification (L), and heatmap of RTPA experiment (M) with $CGRP^{PBel \rightarrow CeA}$ terminal photostimulation. Scale bars, 200 μm.
(N) ChR2-expressing mice, but not EYFP controls, avoided the chamber paired with $CGRP^{PBel \rightarrow CeA}$ terminal photostimulation. n = 5 (EYFP), n = 6 (ChR2) mice. Data are presented as mean ± SEM. Statistical analyses were performed using repeated-measures two-way ANOVA with post hoc Sidak's multiple comparison; see also Table S5 for statistical details. *$p < 0.05$, **$p < 0.01$, ***$p < 0.001$. See also FiguresS5 and S6.

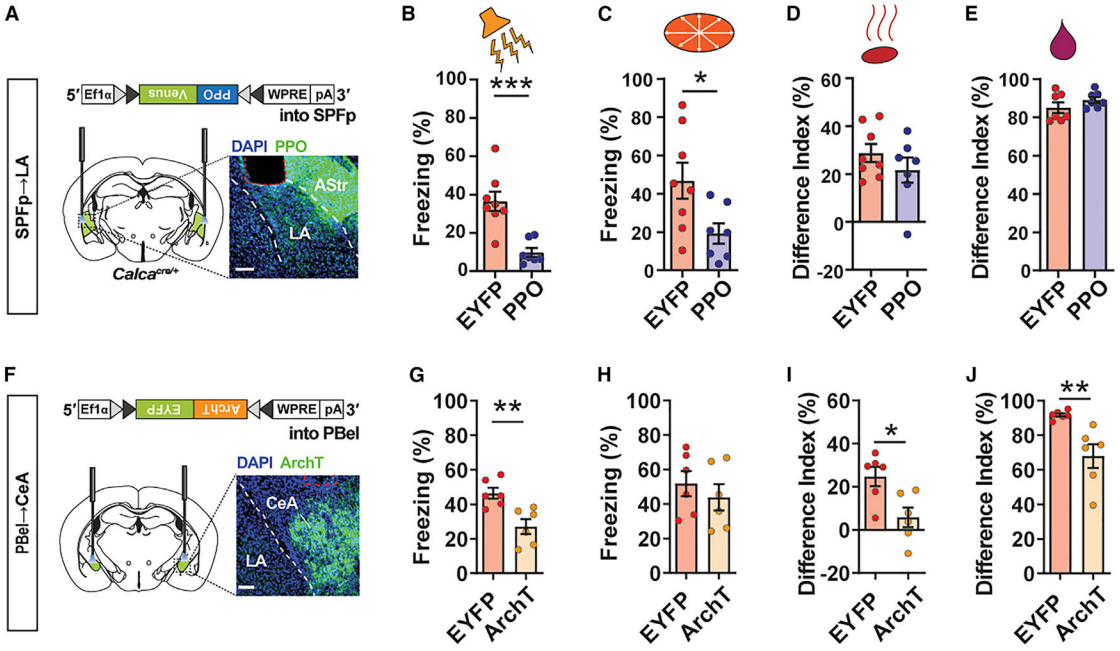

Figure 5. CGRP$^{SPFp→LA}$ and CGRP$^{PBel→CeA}$ projections are required for multi-sensory innate threat perception

(A) Schematic for silencing CGRP$^{SPFp→LA}$ circuit with PPO. Scale bars, 200 μm.

(B–E) Silencing the CGRP$^{SPFp→LA}$ circuit reduced behavioral responses to aversive auditory (B) and visual (C) stimuli, but not olfactory (D) or gustatory (E) stimuli. Auditory, visual, and olfactory: n = 8 (EYFP), n = 7 (PPO) mice; gustatory: n = 7 (EYFP), n = 7 (PPO) mice.

(F) Schematic for silencing CGRP$^{PBel→CeA}$ circuit with ArchT. Scale bars, 200 μm.

(G–J) Silencing the CGRP$^{PBel→CeA}$ circuit reduced behavioral responses to aversive auditory (G), olfactory (I), and gustatory (J) stimuli, but not visual (H) stimuli. n = 6 (EYFP), n = 6 (ArchT) mice.

Data are presented as mean ± SEM. Statistical analyses were performed using two-tailed unpaired t tests; see also Table S5 for statistical details. *p < 0.05, **p < 0.01, ***p < 0.001.

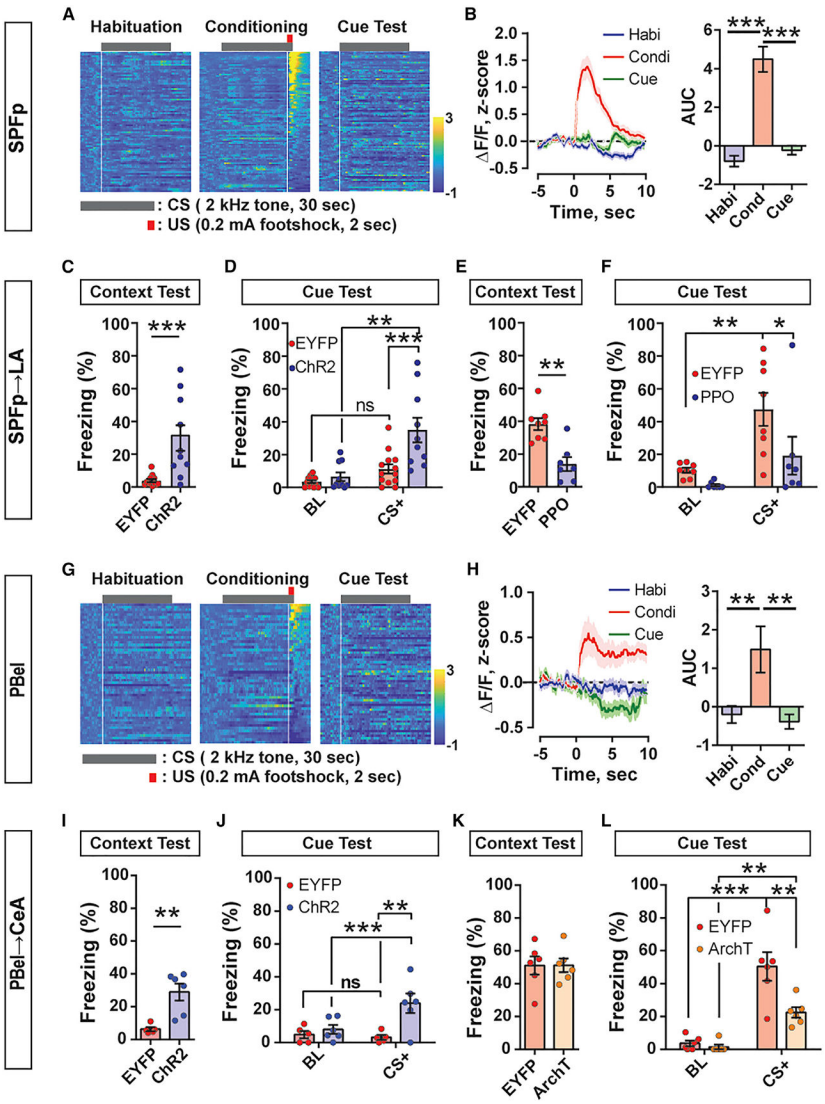

Figure 6. CGRP$^{SPFp→LA}$ and CGRP$^{PBel→CeA}$ circuits relay unconditioned stimulus information and are crucial for aversive memory formation during Pavlovian threat conditioning

(A) Heatmap of Z-scored CGRP^{SPFp} single-cell calcium activity during threat conditioning. n = 81 (habituation), n = 90 (conditioning), and n = 93 cells (cue test) from three mice. Each row represents the averaged value during three to six stimulus presentations in a single cell. White vertical lines indicate the onsets of tone or foot shock used for (B).

(B) Left: averaged peri-stimulus activity of all recorded CGRP^{SPFp} neurons. Stimulus onset is indicated by white vertical lines in (A). Right: area under the curve (AUC) of all recorded CGRP^{SPFp} neurons. AUCs were calculated from 0 to 5 s after stimulus onset. CGRP^{SPFp} neurons were activated by the unconditioned stimulus (foot shock) and not by the conditioned stimulus (non-aversive tone) during habituation or cue tests. n = 81 (habituation), n = 90 (conditioning), and n = 93 cells (cue test) from three mice.

(C and D) During the optogenetic threat-conditioning test wherein CGRP$^{SPFp→LA}$ circuit photostimulation was used as an unconditioned stimulus (US), the ChR2 group displayed higher freezing levels during both the context (C) and cue (D) retrieval tests than EYFP

controls. n = 13 (EYFP), n = 10 (ChR2) mice. “BL” in the cue test indicates freezing during baseline before the first tone was delivered, and “CS+” is the average freezing during the three tones.

(E and F) Inhibiting the $CGRP^{SPFp \rightarrow LA}$ circuit with PPO during threat conditioning reduced freezing level in the context (E) and cue retrieval tests (F). n = 8 (EYFP), n = 7 (PPO) mice.

(G) Heatmap of *Z*-scored $CGRP^{PBel}$ single-cell calcium activity during threat conditioning. n = 56 (habituation), n = 50 (conditioning), and n = 59 cells (cue test) from three mice. White vertical lines indicate the onsets of tone or foot shock used for (H).

(H) Same design as in (B). $CGRP^{PBel}$ neurons were activated by the unconditioned stimulus (foot shock), but not by the cues during either habituation or cue tests. n = 56 (habituation), n = 50 (conditioning), and n = 59 cells (cue test) from three mice.

(I and J) During the optogenetic threat-conditioning test wherein $CGRP^{PBel \rightarrow CeA}$ circuit photostimulation was used as a US, the ChR2 group displayed higher freezing levels during both the context (I) and cue (J) retrieval tests than EYFP controls. n = 5 (EYFP), n = 6 (ChR2) mice.

(K and L) Inhibiting the $CGRP^{PBel \rightarrow CeA}$ circuit with ArchT during threat conditioning reduced freezing behavior in the cue retrieval test (L) but not the context test (K). n = 6 (EYFP), n = 6 (ArchT) mice.

Data are presented as mean ± SEM. Statistical analyses were performed using Kruskal-Wallis one-way ANOVA on ranks with Dunn’s multiple comparisons (B and H), two-tailed unpaired t tests (C, E, I, and K), or repeated-measures two-way ANOVA with post hoc Sidak’s multiple comparison (D, F, J, and L); see also Table S5 for statistical details. *$p < 0.05$, **$p < 0.01$, ***$p < 0.001$. See also Figures S7-S9.

KEY RESOURCES TABLE

REAGENT or RESOURCE	SOURCE	IDENTIFIER
Bacterial and virus strains		
AAV8-hSyn-FLEX-TVA-P2A-GFP-2A-oG	Salk Institute viral vector core	RRID:Addgene_85225
EnvA-ΔG-rabies-mCherry	Osakada et al. (2011), Salk Institute viral vector core	RRID:Addgene_32635
AAV1-DIO-GFP:TetTox	Carter et al. (2015); Han et al. (2015), Laboratory of Dr. Richard Palmiter	N/A
AAV1-DIO-EYFP	Bowen et al. (2020); Han et al. (2015), Laboratory of Dr. Richard Palmiter	RRID:Addgene_27056
AAV-DIO-jGCaMP8m	Zhang et al. (2020), Janelia Viral Vector Core	RRID:Addgene_162378
AAVDJ-EF1a-DIO-hChR2(H134R)-EYFP-WPRE-pA	Karl Deisseroth, Salk Institute Viral Vector Core	RRID:Addgene_20298
AAV5-EF1a-DIO-PPO-Venus	Copits et al. (2021), Laboratory of Dr. Michael Bruchas	RRID:Addgene_139505
AAVDJ-DIO-ArchT-GFP	Han et al. (2011), Salk Institute viral vector core	RRID:Addgene_28307
Deposited data		
Custom MATLAB scripts for data analysis	This paper	Zenodo: https://doi.org/10.5281/zenodo.6667324
Experimental models: Organisms/strains		
Mouse: *Calca*-Cre:GFP	Laboratory of Dr. Richard Palmiter	N/A
Software and algorithms		
MATLAB	MathWorks	R2019a
Ethovision XT	Noldus Information Technology	Version 12
Inscopix Data Processing Software	Inscopix	Version 1.6.0.3225
pCLAMP	Molecular Devices	Version 10
BZ-W viewer	Keyence	N/A
Fluoview	Olympus	N/A
Sigmaplot	Systat Software Inc.	Version 14.0
Prism	GraphPad Software	Version 6
Illustrator	Adobe	Version CS6 and CC2018
Other		
200um 0.22 NA Fiber-optic Cannula	Laboratory of Dr. Sung Han	N/A
ProViewÔ Integrated Lens 0.6 mm × 7.3 mm	Inscopix	Cat# 1050-004413